Ocean Modelling 168 (2021) 101891

Contents lists available at ScienceDirect

Ocean Modelling

journal homepage: www.elsevier.com/locate/ocemod

Relative vs. absolute wind stress in a circumpolar model of the Southern Ocean

David R. Munday [a,*], Xiaoming Zhai [b], James Harle [c], Andrew C. Coward [c], A.J. George Nurser [c]

[a] British Antarctic Survey, Cambridge, UK
[b] School of Environmental Sciences, University of East Anglia, Norwich, UK
[c] National Oceanography Centre, Southampton, UK

ARTICLE INFO

Dataset link: https://www.nemo-ocean.eu, https://doi.org/10.5281/zenodo.4707331, http://dx.doi.org/10.5285/2e982e6692e3427dbe35e64ad9dee12d, https://catalogue.ceda.ac.uk/uuid/67ad0c489e2b4d18aa152e78f28ae0c0, https://catalogue.ceda.ac.uk/uuid/aa4106a7a35246dfb84fb925a7d65650, https://dataverse.harvard.edu/dataverse/ECCOv4r2, https://marine.copernicus.eu, http://www.esa-sst-cci.org/PUG/pug.htm, http://sose.ucsd.edu, https://www.earthsystemgrid.org/dataset/ucar.cgd.asd.cs.hybrid_v5_rel04_BC5_ne120_t12_pop62.ocn.proc.daily_ave.html, https://rda.ucar.edu/datasets/ds093.2, https://nsidc.org/data

Keywords:
Southern Ocean
Mesoscale eddies
Relative wind
Current-wind interaction

ABSTRACT

The transfer of momentum between the atmosphere and ocean is dependent upon the velocity difference between the seawater and overlying air. This is commonly known as relative wind, or ocean current interaction, and its direct effect is to damp mesoscale ocean eddies through the imposition of an opposing surface torque. If an ocean model neglects the ocean velocity in its bulk formulae, this can lead to an increase in power input to the ocean and a large increase in Eddy Kinetic Energy (EKE). Other secondary effects that are dependent upon the current system under consideration may also occur. Here we show that the neglect of relative wind leads to an ~ 50% increase in surface EKE in a circumpolar model of the Southern Ocean. This acts to increase the southwards eddy heat transport, fluxing more heat into the seasonal ice zone, and subsequently reducing ice cover in all seasons. The net reduction in planetary albedo may be a way for a largescale impact on climate.

1. Introduction

The turbulent transfer of momentum between atmosphere and ocean is typically expressed as a surface wind stress, as calculated via a bulk formula parameterisation. This relates the wind stress to the difference between the atmospheric wind, usually at an elevation of 10 m, and the surface ocean velocity:

$$\boldsymbol{\tau}_s = \rho_a c_d \left|\mathbf{U}_{10} - \mathbf{u}_s\right| \left(\mathbf{U}_{10} - \mathbf{u}_s\right), \tag{1}$$

where $\boldsymbol{\tau}_s$ is the surface wind stress, ρ_a is the atmospheric density, c_d is the drag coefficient, $\mathbf{U}_{10}$ is the 10 m atmospheric wind and $\mathbf{u}_s$ is the surface ocean velocity. Note that the drag coefficient may also be a function of $\mathbf{U}_{10} - \mathbf{u}_s$.

The inclusion of the surface ocean velocity in the bulk formula, referred to as "relative wind" or "ocean current interaction/feedback", acts as a source of friction at the ocean surface that directly dissipates mesoscale ocean eddies (Dewar and Flierl, 1987) and equatorial waves (Pacanowski, 1987). Furthermore, there is a substantial difference in the surface power input to the ocean between calculations that use relative wind vs. absolute wind (when the $\mathbf{u}_s$ is neglected in Eq. (1)) for wind stress calculations (Duhaut and Straub, 2006). Estimates of the change in power input differ, but are typically 10–35% of the total (Duhaut and Straub, 2006; Dawe and Thompson, 2006; Hughes and Wilson, 2008; Zhai and Greatbatch, 2007; Zhai et al., 2012; Munday and Zhai, 2015).

The additional friction under a relative wind stress acts to efficiently damp the eddy field, such that the Eddy Kinetic Energy (EKE) is reduced with respect to an absolute wind stress simulation. The exact decrease depends upon the region under consideration. For the California Upwelling System, Renault et al. (2016b) found that surface EKE decreased by ~ 50%, whilst the depth averaged EKE decreased by ~ 27%. Decreases in surface EKE of $\gtrsim$ 25% have also been found for the Gulf Stream and Agulhas Current (Renault et al., 2016a, 2017), as well as the California Current System and Arabian Sea (Seo et al., 2016;

* Corresponding author.
E-mail address: danday@bas.ac.uk (D.R. Munday).

https://doi.org/10.1016/j.ocemod.2021.101891
Received 13 May 2021; Received in revised form 3 August 2021; Accepted 26 September 2021
Available online 1 October 2021

Seo, 2017). Changes in EKE are particularly pronounced in the Bay of Bengal, where a switch between absolute and relative wind can result in a factor of two change (Seo et al., 2019).

The switch to relative wind stress can lead to a more realistic simulation, specifically Renault et al. (2016a) show improved Gulf Stream circulation post-separation and Luo et al. (2005) show improvements in the equatorial Pacific's warm-pool/cold-tongue structure. Other aspects of the eddy field, other than changes to its energy, such as their propagation and lifetime, can also lead to improvements (Renault et al., 2017). The use of coupled atmosphere–ocean models has highlighted that the response of the coupled atmosphere partially mitigates the impact of relative wind stress on EKE. This is due to a slightly increased wind stress, with respect to that achieved by a prescribed atmosphere, leading to a partial re-energisation of the EKE of the ocean (Renault et al., 2016b).

The Southern Ocean (SO) is a region of strong wind forcing in which the mesoscale eddy field plays important roles in its budgets of momentum (Munk and Palmén, 1951; Johnson and Bryden, 1989) and heat (Bryden, 1979; Jayne and Marotzke, 2002; Meijers et al., 2007). The strong winds do considerable work on the ocean due to the prevailing eastward direction of the SO's currents; of the ~ 1 TW of power input to the geostrophic circulation, roughly ~ 0.5 TW takes place in the SO (Wunsch, 1998; Wunsch and Ferrari, 2004; Ferrari and Wunsch, 2009). This has the potential to create a perfect storm in terms of the impacts of relative wind, with the mesoscale eddies being directly damped and the power input to the ocean reduced in a region where both are of first order importance.

The impact of using relative vs. absolute wind stress on SO circulation has been previously explored. Hutchinson et al. (2010) show a 38 Sv increase in the circumpolar transport of a quasi-geostrophic Antarctic Circumpolar Current (ACC) when switching from an absolute to relative wind stress formulation. This occurs due to a weakening of the eddy field and an accompanying steepening of the isopycnals under relative wind stress. In contrast, Munday and Zhai (2015) use a primitive equation, but idealised, channel model of the SO in which the circumpolar transport increases by a more modest 10–15 Sv under relative wind stress due to the same mechanism. Furthermore, they find that the sensitivity of the Residual Meridional Overturning Circulation (RMOC) to changing wind stress is effectively the same under both absolute and relative wind stress. This is due to a cancellation between steepening isopycnal slope and reduced eddy diffusivity under relative wind stress.

Despite the above progress, outstanding questions remain.. For example, Hutchinson et al. (2010) use a coupled quasi-geostrophic model (Q-GCM, see Hogg et al., 2003, although in this case the atmosphere above the boundary layer does not evolve freely). It is subject to simplifications in the governing equations that are not present in the primitive equation model (MITgcm, see Marshall et al., 1993, 1994) used by Munday and Zhai (2015). However, it benefits through the inclusion of complex bathymetry, albeit vertically truncated to ± 780 m above a mean ocean depth of 4000 m. The idealised domain of Munday and Zhai (2015) is flat-bottomed, which results in a zonally-symmetric mean state that is not subject to concentration of eddy activity behind bathymetric obstacles. Neither study includes variability in the atmospheric forcing or sea ice, which excludes a potentially important feedback on circulation changes. The $1/20°$Drake Passage model of Song et al. (2020) also uses MITgcm, this time in a realistically complex model domain with untruncated bathymetry. In their case, use of relative wind results in a 24% drop in EKE with respect to an absolute wind run of the same model. This is comparable to that found in other regions of the ocean (see above). However, it is spatially limited to $140°$ of longitude and may be subject to additional limitations from its lateral boundary conditions.

This paper aims to investigate the differences between the use of relative and absolute wind stress in a circumpolar model of the SO that includes realistically complex bathymetry and time-varying forcing via the use of reanalysis products. This model includes a coupled sea-ice component. In Section 2, we describe the fundamentals of the model configuration and surface forcing (Section 2.2). In Section 3 we briefly review the large scale circulation of our experiments. We break our discussion of the model results into Section 4 on wind power input, Section 5 on EKE, Section 6 on meridional heat transport, and on sea ice extent/area and the sea ice seasonal cycle. We end the paper with a summary and discussion in Section 8.

2. Model setup and data sources

2.1. NEMO model configuration

We use a circumpolar configuration of NEMO, the Nucleus for European Modelling of the Ocean, coupled to LIM3, the Louvain-La-Neuve sea ice model (Vancoppenolle et al., 2009; Rousset et al., 2015). Due to the time period during which this configuration was developed, our NEMO-LIM revision is intermediate between that of the previous release (v3.6) and that of the current NEMO-LIM release (v4.0 NEMO System Team, 2019). It incorporates some bugfixes and code developments made as part of v4.0. The model's horizontal grid spacing is $1/12°$, to allow for a vigorous mesoscale eddy field, and there are 75 levels spread unevenly through the water column. We make use of the z-star vertical coordinate system (Adcroft and Campin, 2004) with partial vertical steps (Adcroft et al., 1997) and the thermodynamic equation of state for seawater (TEOS-10, e.g. Roquet et al., 2015). There is no sea surface restoring to either temperature or salinity. The model is run on 2542 cores with land suppression active, which eliminates roughly half of the model domain (without land suppression 4944 cores would be required), and a timestep of 300 s.

To the south the ocean is bounded by the Antarctic continent and the latitude of the northern boundary is staggered in each ocean basin. This is to accommodate a second version of the model, currently in development, that incorporates a new hybrid vertical coordinate, ice shelves and, potentially, tides. The northern boundary has been moved to avoid being too close to tidal amphidromes, which can lead to spurious generation of tidal energy. In the Atlantic basin, the northern boundary is at $7.27°$S, whilst it is at $22.83°$S and $29.04°$S in the Indian and Pacific basins, respectively. The positions of the amphidromes, and thus the position of the northern boundary, was determined with a test of the current configuration that included tides (not shown).

At the northern boundary we strongly restore to an annual climatology from the ECCOv4r2 state estimate (Forget et al., 2015, 2016). The initial state of the model is taken as January of this climatology. ECCOv4r2 has a small misfit to observations and is an optimal estimate of the ocean's circulation over the period 1992 to 2011. By using a state estimate-derived climatology we avoid inheriting modelling issues resulting from, e.g., a global model and being limited to the run length of this parent model. Note that we have to transform the potential temperature and practical salinity of ECCO4v2 to conservative temperature and absolute salinity for use with TEOS-10. At the northern boundary a Flather condition is applied to the barotropic flow and a Neumann condition to the baroclinic flow. Temperature and salinity are restored as per the flow relaxation scheme (Davies, 1976; Engerdahl, 1995) over a 24 gridbox-wide sponge.

The lateral boundaries use freeslip boundary conditions for momentum and we make use of the vector invariant form of the momentum equation. The Hollingsworth et al. (1983) correction is applied to the KE term, since it can otherwise give rise to spurious energy (Bell et al., 2016). The Coriolis acceleration is calculated using the energy and enstrophy conserving form. Over the global ocean this is known to reduce noise in the vertical velocity (Le Sommer et al., 2009) and, when combined with partial vertical steps, improves flow-topography interaction (Barnier et al., 2006; Penduff et al., 2007). A split-explicit scheme, following that of Shchepetkin and McWilliams (2005), is used

to solve the free surface equation. The horizontal viscosity is biharmonic with a coefficient equivalent to 1.25×10^{10} m^4 s^{-1} at the Equator. The biharmonic viscosity is scaled by the model grid spacing and so varies with latitude.

For the advection of temperature, salinity and age tracers, we use the MUSCL scheme (van Leer, 1979). The choice of tracer advection scheme can influence a model's circulation in profound ways (Gerdes et al., 1991; Griffies et al., 2000). Complex advection schemes, such as that due to Prather (1986), may lead to improvements in the modelled circulation (Hofmann and Morales Maqueda, 2006; Morales Maqueda and Holloway, 2006). MUSCL is an upwind-biased scheme that is relatively cheap in computational terms. There are persuasive arguments of the benefits of such schemes with respect to the over- and under-shoots that may be experienced with dispersive schemes, typically centred in nature (van Leer, 1973, 1974, 1977a,b, 1979, 1997; Hecht et al., 1995). The diffusion on the tracer fields is Laplacian in nature and applied along isopycnals (e.g. Redi, 1982) with a coefficient equivalent to 125 m^2 s^{-1} at the Equator. The Laplacian viscosity is scaled by the model grid spacing and so varies with latitude.

At each timestep the total freshwater flux, i.e. evaporation minus precipitation minus runoff and including contributions from ice shelf runoff, but excluding flow through the northern boundary and sea ice growth/melt, is set to zero via a uniform correction applied to the area integrated evaporation minus precipitation. This correction will not be an accurate representation of the freshwater forcing, i.e. over a seasonal cycle the Southern Ocean may gain or loss freshwater. However, it prevents any slight imbalance leading to an increase/decrease of volume in the ocean component or a long-term salinity drift. As a result, surface freshwater fluxes are really a redistribution of freshwater within the model domain, rather than a net gain or loss. Rainfall is as provided by the surface forcing set, see Section 2.2, with the evaporation as determined by bulk formula. The sea-ice component is LIM3, coupled to NEMO at every timestep, and using the 5th order Ultimate-Macho advection scheme and no diffusion. The ice levitates on the sea surface and exchanges mass and salt with no pressure effect. There are five ice categories, two ice layers and one snow layer.

Advective and diffusive bottom boundary layer parameterisations are applied to improve the connection between non-adjacent bottom cells. The momentum equations are additionally subject to nonlinear bottom friction with a spatially-varying coefficient. Vertical mixing processes are represented by a TKE scheme based on that of Blanke and Delecluse (1993). We have adopted a number of modelling options from configurations of the UK Met Office. In particular, bottom enhanced tidal mixing on the eORCA12 grid, associated with the K1 and M2 tide, is applied as per Simmons et al. (2004) and a climatological geothermal heat flux from Goutorbe et al. (2011) is applied at the sea bed. Rather than use the runoff from the specific forcing sets (we do not intend to follow the established protocols of the forcing sets), we use river and iceshelf runoff provided by the Met Office. This is adapted to our high resolution grid and shoreline. The iceshelf runoff is vertically spread over 10 m.

The model includes a pair of age tracers, which are subject to the same advection–diffusion schemes as temperature and salinity (see above). The first tracer is set to zero within the northern boundary sponge for the flow relaxation scheme. Outside of this sponge it ages at a rate of 1 s/s. It measures the age relative to water that has just entered/left the domain at the northern boundary. The second age tracer is set to zero near the northern boundary and within 10 m of the surface. It measures the age of the water relative to both these locations and so conflates multiple sources of information. We take this approach due to numerical issues near the northern boundary that lead to the generation of spurious values for unconstrained age tracers. An alternative would have been to provide an age value appropriate to ECCOv4r2 at the northern boundary. However, no such profile was available at the time of running the model. The combination of the two tracers help disentangle surface subduction from entry into the domain via the northern boundary.

2.2. Surface forcing

We have performed three experiments. The first of these is a control run using the CORE2 normal year forcing (Large and Yeager, 2004, 2009) for 40 years (referred to as CORE2NYF Munday et al., 2021), note that this does not include leap days. This is used to spinup an initial eddy field and circulation without biasing it towards a specific calendar year. The nominal start date for this control run is 1948, with the stratification reset to ECCOv4r2 conditions at the beginning of January of 1949 and 1950. This initialisation period allows us to start in January with no sea ice whilst preventing the generation of overly-saline water within the seasonal ice zone. CORE2NYF nominally ends on 31 December 1987. Results presented from CORE2NYF are largely from the last five years (1 January 1983 to 31 December 1987).

The second control run is forced by JRA55-do interannually-varying forcing (Tsujino et al., 2018) and is also run for 40 years (referred to as JRA55IAF Munday et al., 2021). Note that the JRA55-do forcing does include leap days and benefits from an increased horizontal ($\sim$ 55 km) and temporal resolution (3 hr), with respect to CORE2. JRA55IAF is started on 1 January 1978 from a restart of CORE2NYF and runs until 31 December 2017. This provides an already energetic eddy field and helps mitigate the additional spinup due to changing forcing set. The third experiment uses the JRA55-do forcing under an absolute wind stress condition (referred to as JRA55ABS Munday and Zhai, 2021). This experiment is 20 years long and starts on 1 January 1988 from a restart of JRA55IAF. This allows a 10 year adjustment to the change from CORE2NYF to JRA55IAF and maintains an overlapping control run for the life of JRA55ABS. The switch to absolute, instead of relative, wind stress also removes the impact of the ocean velocity on other fluxes through the bulk formulae. The majority of our presented results from JRA55IAF and JRA55ABS are from 1 January 2003 to 31 December 2007. This corresponds to the last five years of JRA55ABS and ensures that both JRA55-do-forced models have comparable atmospheric forcing. We have also examined the 1983–1987 and 2013–2017 averages for JRA55ABS and whilst the quantitative detail changes our conclusions do not.

In initial tests with CORE2 normal year forcing it was found that beyond an integration threshold of $\sim$ 12 years, the model would generate a large Weddell Sea polynya. Due to thermal wind shear this led to acceleration of the Antarctic Circumpolar Current and ultimately numerical instability. In order to suppress polynya formation, we followed the guidance of Kjellson et al. (2015) and added additional freshwater to the prescribed runoff. To do so we triple the amount of prescribed runoff to include an additional 2500 Gt/yr and also include an additional 1500 Gt/yr south of 60°S, to simulate iceberg melt. This additional freshwater is still subject to the constraint that the area-integrated freshwater flux be zero at every timestep and so remains a redistribution of freshwater rather than strictly an extra volume. The extra flux suppresses the polynya throughout the 40 years of CORE2NYF allowing a stable ocean circulation to develop. In order to maintain comparability between the two control runs, we also maintain this additional freshwater forcing in JRA55IAF and JRA55ABS. The formation process of the Weddell Sea polynya is described in Appendix A.

2.3. Data sources

To provide an estimate of EKE, we make use of altimetry from the Archiving, Validation and Interpretation of Satellite Oceanographic data (AVISO) in the form of daily level 4 reprocessed derived variables from 1/1/2003 to 12/31/2007. The product has been processed by SSALTO/DUACS to merge all flying altimeters via optimal interpolation onto a regular 1/4° grid. We use absolute geostrophic velocities derived from absolute dynamic topography to calculate the EKE.

Sea ice area and extent data are taken from the National Snow and Ice Data Center (NSIDC). Satellite derived sea ice extent is provided by

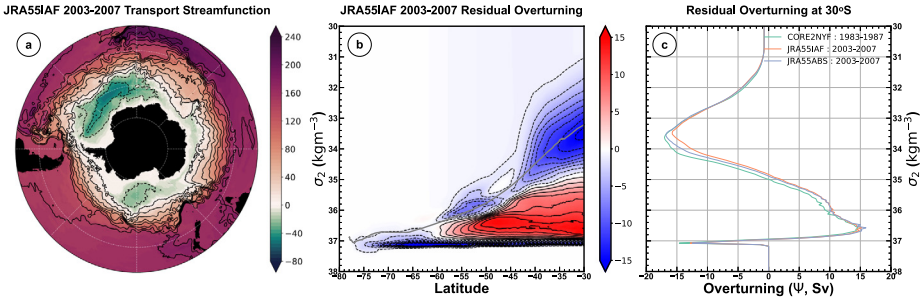

Fig. 1. The modelled large-scale circulation of the ocean for JRA55IAF. (a) Transport streamfunction in Sv averaged over 2003–2007. Solid black is land. Only the model domain south of 35°S is shown. (b) Residual overturning streamfunction, using density referenced to 2000 m for the vertical coordinate, in Sv. The grey line is the zonally-averaged surface density. (c) Residual overturning streamfunction at 30°S as a function of density. The data sources and time periods are as per the panel legend.

the NSIDC sea ice index v3 (Fetterer et al., 2017, updated daily). This combines Nimbus-7 SMMR and DMSP SSM/I-SSMIS Passive Microwave Data satellite images to generate daily and monthly images. The sea ice index runs from November 1978 to present; we use an average from 1983 to 2010. We also use monthly averages of sea ice concentration as a spatial field (Cavalieri et al., 1996, updated yearly).

3. Large-scale circulation

The zonal circulation of all three models is dominated by the ACC over much of the model domain, as per the transport streamfunction in Fig. 1a for JRA55IAF, which is representative of all three models. Subtropical gyres are present in the Atlantic and Indian basins, with the Brazil and Agulhas Currents interacting with the ACC north of the Falkland Islands and south of Cape Agulhas, respectively. Due to the placement of the northern boundary, the wind-driven gyre to the east of Australia and New Zealand is particularly weak and there is little signature of the East Australia Current (EAC) present. In this sector of the model, the northern boundary is at 29.04°S, which is very close to the latitude of Sugarloaf Point, where the EAC leaves the coast of Australia and flows towards New Zealand. As such, the model domain is excluding most of its formation region and the result is a very weak current. In these broad strokes, the models are largely very similar. There are differences in, e.g., the position and intensity of the Brazil–Malvinas Confluence or the strength of the Agulhas Current. However, the result is a credible simulation of the Southern Ocean horizontal circulation inline with other models of similar resolution, see, e.g. Mazloff et al. (2010) and Delworth et al. (2012), etc.

The volume transport through Drake Passage, T_{ACC}, is a commonly taken metric of the zonal flow of the Southern Ocean. Recent observational estimates give a transport of 136.7 ± 6.9 Sv (Meredith et al., 2011), based on analysis of historical hydrographic sections, and 173.3± 10.7 Sv (Donohue et al., 2016), which includes the barotropic flow. For all three models we calculate T_{ACC} using five day averages of the product of the zonal velocity and level thickness across Drake Passage. We take a five year average value over 1983–1987 for CORE2NYF and 2003–2007 for JRA55IAF and JRA55ABS. We use the standard deviation of the five day mean values over these time periods as a measure of variability. Due to model spinup, internal variability of the ocean and variability in the surface forcing (for JRA55IAF and JRA55ABS), the particular five year period chosen for the average value can lead to changes in both the mean and standard deviation of T_{ACC}.

T_{ACC} for all three experiments is intermediate between the observational estimates of Meredith et al. (2011) and Donohue et al. (2016). For CORE2NYF the transport is 151.58 ± 5.14 Sv (where the uncertainty indicates the standard deviation of all five day means contributing to the average). For JRA55IAF and JRA55ABS the transport is 147.57 ± 5.78 Sv and 147.58 ± 5.68 Sv, respectively. Given the variability in the model these values are largely indistinguishable. Based on the results of Hutchinson et al. (2010) and Munday and Zhai (2015), we would expect to see a larger difference in the Drake Passage transport of JRA55IAF and JRA55ABS. Specifically, we would expect that the relative wind damping of the mesoscale eddy field in JRA55IAF would lead to steeper isopycnals and therefore an increased Drake Passage transport due to thermal wind shear. The lack of an increased transport may be due to a number of affects. Firstly, the model runs are all short. In a timeframe of a few decades, we would not expect the stratification of the ocean to reach its new equilibrium, especially given the spinup time of the ocean's baroclinic structure (Wunsch and Heimbach, 2008; Allison et al., 2011). With ∼ 80% of T_{ACC} due to thermal wind shear, it is reasonable to expect its adjustment time to be dictated by the baroclinic, rather than barotropic, mode. Secondly, it could reflect the increase in complexity of the model bathymetry, relative to that of Hutchinson et al. (2010) and Munday and Zhai (2015). With complex, untruncated, bathymetry the models under consideration here may have a fundamentally different response to those previously employed. Thirdly, the surface forcing used here varies strongly in time, in contrast to the constant forcing of both Hutchinson et al. (2010) and Munday and Zhai (2015). Variable wind stress alters the sensitivity of both T_{ACC} and the RMOC to wind stress via changes in near-surface mixing (Munday and Zhai, 2017). To unravel whether the Drake Passage transport of JRA55IAF and JRA55ABS would differ substantially at equilibrium would require a minimum of several hundred model years of further integration, which is beyond the available computing resources. In-depth investigations into the role of complex bathymetry and surface forcing variability are beyond the scope of the current paper.

Both the mean wind stress and the mesoscale eddy field of the Southern Ocean play first order roles in setting its average meridional circulation. In the zonal integral sense, the RMOC is a small difference between much larger individual components determined by the wind stress and the eddy field; the Eulerian overturning, set by the wind stress, and the bolus overturning, set by the eddy field (Marshall and Radko, 2003). These give rise to a two cell structure for the RMOC (Marshall and Speer, 2012) in which mesoscale eddies play an active role due to their capacity to dynamically interact with the stratification of the ocean (Marshall et al., 2002; Karsten et al., 2002). The two cells are usually identified with the clockwise circulation of North Atlantic Deep Water (NADW) overlying anticlockwise circulating Antarctic Bottom Water (AABW).

There are subtleties to the calculation of the RMOC due to the impacts of different forms of averaging (Nurser and Lee, 2004a,b). We diagnose the RMOC using density as the vertical coordinate by rebinning the meridional velocity into 160 density layers that are 0.05 kg m^{-3} thick. Due to modelling constraints, this is done as an offline post-processing calculation using five year's worth of five day means. We calculate the density, referenced to 2000 m, using the five day mean temperature/salinity and TEOS-10, before using the 3D field to rebin the velocity and integrating. The result is shown in Fig. 1b, for JRA55IAF. The expected two cell structure is clear, although the AABW cell is over a narrow range of density, with the flow below the mixed layer being largely adiabatic. Due to the use of five day means

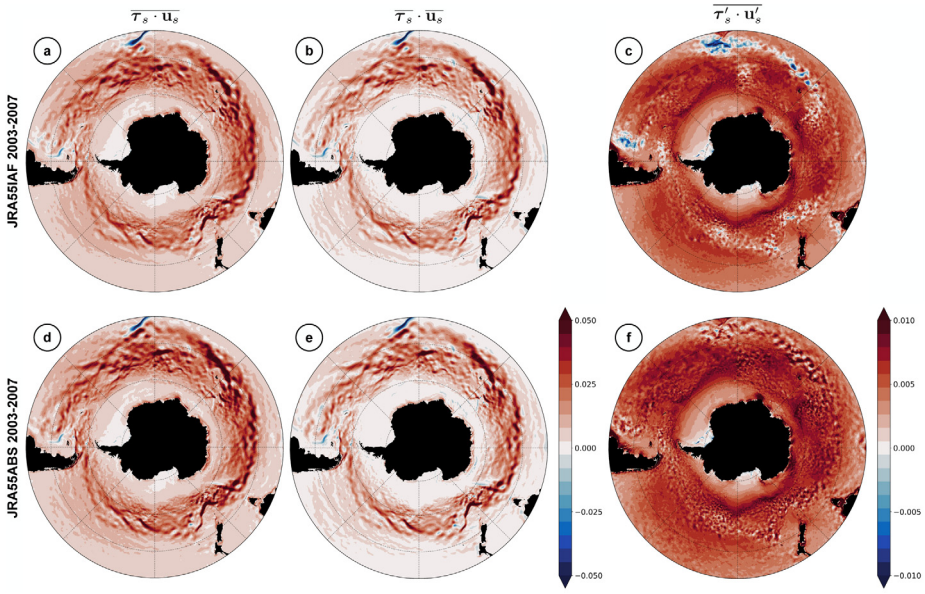

Fig. 2. Reynolds averaged wind power input to the ocean circulation in W m^{-2} for JRA55IAF (upper row) and JRA55ABS (lower row). (a,d) Total wind power input, (b,e) mean power input and (c,f) eddy power input. Time averaging is over the calendar years 2003–2007 for both models. Note the change in colour bar for panels (c) and (f). Solid black is land. Only the model domain south of 35°S is shown.

for the calculation, both for the advection field and for the calculation of density, there will be some slight misallocation of transport between density classes in our RMOC calculation. In addition, variability at frequencies higher than 1/(5 days) will be averaged away and this will lead to a reduction of the bolus overturning. The non-zero values at the low densities are due to the surface freshwater flux. The surface value of the RMOC at each latitude matches the freshwater flux accumulated from the southern boundary to that latitude, as expected.

As a quantitative comparison of the overturning between the three models, we plot the density profile of the RMOC streamfunction at 30°S in Fig. 1c. This is a common latitude for such comparisons, see, e.g., Morrison et al. (2011). At densities greater than ∼ 1037 kg m^{-3} all three models have a similarly narrow AABW cell, implying that this is a property of the general model configuration, rather than of the surface forcing. For CORE2NYF this cell transports 14.62 Sv of water, which is slightly stronger than the 12.83 Sv and 12.49 Sv transported by JRA55IAF and JRA55ABS, respectively. Between densities of around 1035 kg m^{-3} and 1037 kg m^{-3} the models have their NADW cell, with all three being comparable in strength at ∼ 15 Sv. Near the surface, at densities lighter than ∼ 1035 kg m^{-3}, all three models show the presence of a relatively intense surface cell with a peak transport of ∼ 16–17 Sv. This cell is most likely a directly wind-driven Ekman cell and is beyond the scope of this paper. The increase in strength of this cell from JRA55IAF to JRA55ABS is consistent with the slight increase in mean wind stress under absolute wind stress.

In summary, the large-scale circulation of all three models is broadly similar and in-line with other ocean models of similar grid-spacing, forcing, etc. We do not find a significant difference in Drake Passage transport or residual MOC. The first is something of an anomaly, given differences between previous relative and absolute wind driven experiments. This may be due to length of the model runs not allowing for sufficient modification of isopycnal slopes, although fundamental differences in model formulation may also play a role. The lack of significant differences between the RMOC of JRA55IAF and JRA55ABS is consistent with the hypothesis that the length of the model run has not allowed for major change in isopycnal slope and flow. It is also consistent with the results of Munday and Zhai (2015), which show no large differences in sensitivity of the RMOC to changes in surface wind stress under relative/absolute wind stress.

4. Wind power input

The single largest input of power to the ocean is from atmospheric wind (Wunsch and Ferrari, 2004; Ferrari and Wunsch, 2009). Observational estimates of the wind power input are usually constructed from the geostrophic flow using altimetry. Such estimates suggest that global power input is ∼ 1 TW or less (Wunsch, 1998; Hughes and Wilson, 2008; Scott and Xu, 2009), with the exact figure depending upon subtleties such as the inclusion of high frequency winds (Zhai et al., 2012). Roughly half of this wind power input occurs in the Southern Ocean, where strong westerly winds align with strong eastward surface currents (Roquet et al., 2011). Considerably more power is thought to be input to the ageostrophic circulation and surface waves, with estimates reaching 3 TW (Wang and Huang, 2004a) and 60 TW (Wang and Huang, 2004b), respectively. Much of this extra power does little to drive the actual circulation. For example, ∼ 70% of the near-inertial energy input from the wind is dissipated in the upper 200 m (Zhai et al., 2009).

Using our different model runs we calculate two estimates of wind power input. The first of these uses the model's full surface ocean

Table 1
Power input using every timestep in TW. Brackets are values using 1 day means, for comparison with the geostrophic power input figures in Table 2.

Experiment	Years	Total power input	Mean power input	%	Eddy power input	%	Eddy power input, ocean depth > 1000 m
CORE2NYF	1983–1987	0.957 (0.859)	0.614	64.1	0.343 (0.245)	35.9 (28.5)	0.314 (0.222)
JRA55IAF	1983–1987	1.130 (0.944)	0.640	56.6	0.490 (0.304)	43.4 (32.2)	0.454 (0.278)
	2003–2007	1.151 (0.960)	0.654	56.8	0.497 (0.306)	43.2 (31.9)	0.460 (0.279)
	2013–2017	1.195 (0.997)	0.690	57.8	0.505 (0.307)	42.2 (30.8)	0.469 (0.280)
JRA55ABS	2003–2007	1.274 (1.064)	0.692	67.5	0.582 (0.372)	32.5 (34.9)	0.542 (0.342)

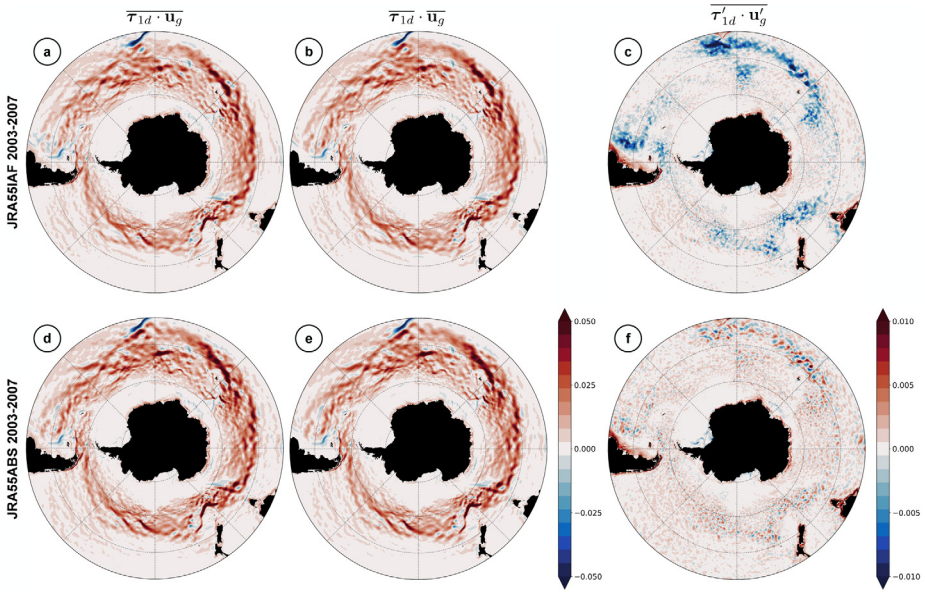

Fig. 3. Reynolds averaged geostrophic wind power input to the ocean circulation in W m^{-2} for JRA55IAF (upper row) and JRA55ABS (lower row). (a,d) Total wind power input, (b,e) mean power input and (c,f) eddy power input. Time averaging is over the calendar years 2003–2007 for both models. Note the change in colour bar for panels (c) and (f). Solid black is land. Only the model domain south of 35°S is shown.

current and a five year average is calculated using every timestep of the model. We use Reynolds averaging to split this into the mean power input and the eddy power input

$$\overline{\boldsymbol{\tau}_s \cdot \mathbf{u}_s} = \overline{\boldsymbol{\tau}_s} \cdot \overline{\mathbf{u}_s} + \overline{\boldsymbol{\tau}'_s \cdot \mathbf{u}'_s} \tag{2}$$

where $\boldsymbol{\tau}_s$ is the surface wind stress, $\mathbf{u}_s$ is the surface ocean current, overbars indicate a five year time average and primes deviations from that average. The second estimate uses a series of one day averages of the surface wind stress and the one day average sea surface height to estimate the geostrophic current. Using Reynolds averaging, we again split this into the mean geostrophic power input and the eddy geostrophic power input

$$\overline{\boldsymbol{\tau}_{1d} \cdot \mathbf{u}_g} = \overline{\boldsymbol{\tau}_{1d}} \cdot \overline{\mathbf{u}_g} + \overline{\boldsymbol{\tau}'_{1d} \cdot \mathbf{u}'_g} \tag{3}$$

where $\boldsymbol{\tau}_{1d}$ is the one day averaged surface wind stress. The estimate of the geostrophic surface currents, $\mathbf{u}_g$, is calculated from the one day average sea surface height

$$\mathbf{u}_g = \frac{g}{f}\mathbf{k} \times \nabla \eta_{1d} \tag{4}$$

where $g = 9.80665$ m s^{-2} is the gravitational acceleration in NEMO, f is the Coriolis frequency, and η_{1d} is the one day average sea surface height.

The spatial pattern of the total power input for both JRA55IAF and JRA55ABS reflects the dominant westerly wind over the eastward currents of the Southern Ocean (see Fig. 2a,d). Energy is input over much of the model domain. In a few locations, most obviously over the Agulhas current, energy is instead extracted from the ocean by the wind. This is due to the mean flow opposing the mean wind stress, as can be clearly seen in the mean power input of Fig. 2b,e. There is little obvious qualitative difference between the total and mean power input of the two experiments. In addition, because the change from relative to absolute wind does not significantly impact the magnitude of the mean wind, or the mean ocean current, there is little clear difference between the mean power input of JRA55ABS with respect to JRA55IAF.

Reynolds averaging reveals that there are more obvious differences in the eddy power input between JRA55IAF and JRA55ABS. In Fig. 2c,f the colour bar has been constrained to better show the detail. Over the Agulhas current, and its extension across the Indian Ocean sector, Fig. 2c shows power loss from the ocean. There is also powerloss from the ocean over the Falklands current. This power loss is largely absent from JRA55ABS in Fig. 2f. Whilst this is symptomatic of the expected damping of the eddy field under relative wind stress in JRA55IAF, the use of the full velocity disguises this damping. We shall return to this below, when considering the geostrophic power input.

The total power input using the full velocity is of order 1.1–1.2TW for JRA55IAF. Due to the interannual variation in the forcing, the specific 5 year period used for the average matters. For example, as per Table 1, 2013–2017 is a particularly windy period in JRA55-do and so the power input to the ocean is 1.195 TW, compared to 1.12TW during 1983–1987. As expected, the use of absolute wind in JRA55ABS leads to an increase in the power input to the ocean for 2003–2007. Relative to JRA55IAF, the increase from 1.151TW to 1.274TW is ∼ 10%, which is somewhat lower than the reported ∼ 20–35% in the literature (Duhaut and Straub, 2006; Hughes and Wilson, 2008; Zhai and Greatbatch, 2007; Zhai et al., 2012). Any variation in the total power input for CORE2NYF is purely due to internal variability of the ocean. As such, the total power input does not vary much around the figure of 0.957 TW in Table 1. Whilst the eddy power input is typically lower in magnitude than the mean power input, its distribution is also less localised in

Table 2
Geostrophic power input in TW using daily means.

Experiment	Years	Total power input	Mean power input	%	Eddy power input	%	Eddy power input, ocean depth > 1000 m
CORE2NYF	1983–1987	0.448	0.470	104.9	−0.022	−4.9	−0.033
JRA55IAF	1983–1987	0.459	0.478	104.0	−0.018	−4.0	−0.031
	2003–2007	0.468	0.484	103.5	−0.016	−3.5	−0.029
	2013–2017	0.492	0.510	103.7	−0.018	−3.7	−0.030
JRA55ABS	2003–2007	0.560	0.519	92.5	0.042	7.5	0.027

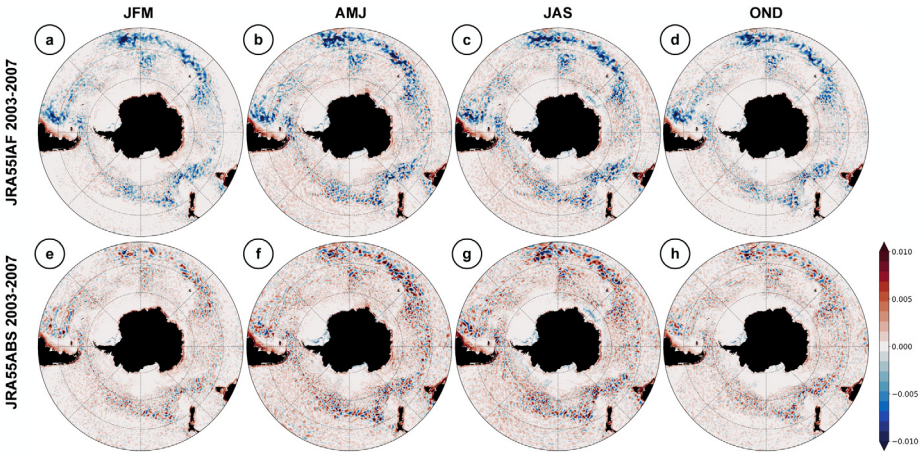

Fig. 4. Geostrophic eddy wind power input to the ocean circulation in W m^{-2} for JRA55IAF (upper row) and JRA55ABS (lower row) as a series of seasonal averages. The mean wind and mean surface ocean current are redefined on a seasonal basis. (a,e) January–February–March average, (b,f) April–May–June average, (c,g) July–August–September average and (d,h) October–November–December average. Time averaging is over the calendar years 2003–2007 for both models. Solid black is land. Only the model domain south of 35°S is shown.

space. As a result, the eddy power input makes up roughly 30–40% of the total, with the exact percentage depending upon the details of the particular experiment and its forcing.

There is a very strong correlation between short-term fluctuations in the wind, inertial oscillations and other high frequency ageostrophic motions. As a result, the eddy power input is dominated by these motions and the expected damping of the mesoscale eddy field is disguised. In order to tease out this damping, we use the method of Wu et al. (2017) and Renault et al. (2016a) and Renault et al. (2017) and use daily mean SSH fields to calculate the surface geostrophic flow, as per Eq. (4). This is then combined with daily wind averages to estimate the geostrophic power input, as per Eq. (3). The result, and its decomposition into geostrophic mean and geostrophic eddy power inputs, is shown in Fig. 3.

The geostrophic total and geostrophic mean power input for both JRA55IAF and JRA55ABS in Figs. 3a,b,d,e are qualitatively very similar to that obtained with the full velocity in Figs. 2a,b,d,e. The broad strokes of the most intense values being over the ACC and lower power input to the north and south remain true. Likewise, there is power loss over the Agulhas and Falklands current regions. There is a general reduction in magnitude, most clearly seen outside of the ACC, such that the total power input to the geostrophic flow is ∼ 0.45–0.56 TW, compared to ∼ 1.0–1.3 TW for the full velocity. This is comparable to observational estimates of Wunsch and Ferrari (2004) and Ferrari and Wunsch (2009), which place the power input at ∼ 0.5 TW for the Southern Ocean. Furthermore, it suggests that somewhere in the region of 0.5–0.6TW is fed into near-surface ageostrophic motions and/or mixing processes. A large part of the surface ageostrophic flow is probably due to Ekman transport. Whilst the net Ekman transport is expected to be at a right angle to the wind, and thus cannot contribute to its power input, this need not be the case for the surface current. The percentage increase in geostrophic power input from JRA55IAF to JRA55ABS is ∼ 20%, which compares well to values previously quoted in the literature (Duhaut and Straub, 2006; Hughes and Wilson, 2008; Zhai and Greatbatch, 2007; Zhai et al., 2012).

The real difference in using the geostrophic velocity to estimate the power input is brought out in the geostrophic eddy power input, as seen in Figs. 3c,f (note the change in the colour bar, which highlights the regions of power loss). For JRA55IAF, which uses relative wind stress, there is clear power loss in regions of high EKE. In particular, the Agulhas current region and its extension, north of the Falklands, south of Australia and New Zealand and near other regions of bathymetry extending high into the water column. Broadly speaking, the spatial pattern of power loss reflects the EKE (see Section 5), as one would expect given that relative wind is expected to directly damp mesoscale eddies. In contrast, JRA55ABS, which uses absolute wind, lacks these large areas of power loss. Within the core of the ACC, there are instead small regions of both positive and negative power input, which highlights the lack of mesoscale damping from absolute wind stress. However, positive values in coastal areas around Australia, New Zealand, Argentina and Chile persist. In these shelf regions the model EKE is low (see Section 5), which may mean that there are insufficient eddies for the damping effect of relative wind stress to be significant.

As shown in Table 2, the integral of the geostrophic eddy power input over the whole domain is negative for CORE2NYF and JRA55IAF and the figure of $\lesssim -0.02$TW is ∼ 4% of the total geostrophic power input. Broadly speaking, it is an order of magnitude less than the eddy power input using the full velocity, as shown in Table 1. For JRA55IAF the power loss is somewhat low compared to the observational estimate of −0.0257 TW for the Southern Ocean (Hughes and Wilson, 2008). However, if we exclude the shelf regions, noted to have high power input in our model and which the altimeter may not represent well in Hughes and Wilson (2008), we instead estimate a figure of ∼ −0.03 TW for water deeper than 1000 m, which compares

Table 3
Seasonal decomposition of geostrophic power input in TW using daily means.

Experiment	Season	Total power input	Mean power input	Eddy power input			Max. τ_x (N m^{-2})
				Total	<0	>0	
JRA55IAF	JFM	0.405	0.426	−0.021	−0.056	0.035	0.215
	AMJ	0.506	0.515	−0.009	−0.069	0.060	0.334
	JAS	0.536	0.550	−0.014	−0.070	0.057	0.339
	OND	0.422	0.443	−0.020	−0.060	0.040	0.242
JRA55ABS	JFM	0.487	0.458	0.029	−0.035	0.064	0.223
	AMJ	0.603	0.554	0.048	−0.051	0.099	0.312
	JAS	0.640	0.594	0.046	−0.052	0.098	0.335
	OND	0.511	0.480	0.031	−0.039	0.070	0.246

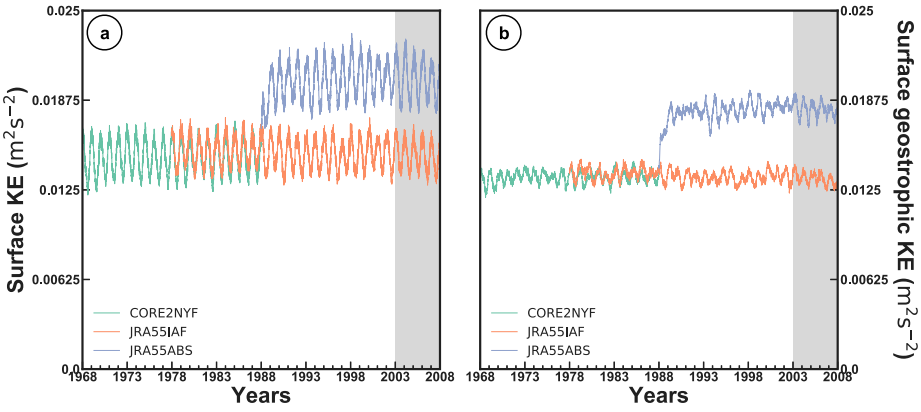

Fig. 5. Time series of surface average kinetic energy built using (a) squared daily means of velocity (b) daily means of SSH to reconstruct the geostrophic velocity as per Eq. (4). The grey shading highlights the time-averaging period used for JRA55IAF and JRA55ABS for subsequent figures.

well to their figure of −0.0257 TW. In contrast to the experiments with relative wind stress, the area integrated geostrophic eddy power input estimate of JRA55ABS is 0.042 TW. Excluding the shelf regions reduces the magnitude to 0.027 TW, with the difference between the two estimates being roughly the same as for CORE2NYF and JRA55IAF, i.e. the positive power input over the shelf regions is broadly the same regardless of the use of relative wind stress. The overall positive value is to be expected for JRA55ABS because the source of additional friction due to relative wind stress has been removed.

The use of one day averages for the geostrophic power input estimate will tend to affect the total power input ($\overline{\boldsymbol{\tau}_{1d} \cdot \mathbf{u}_g}$) and the eddy power input ($\overline{\boldsymbol{\tau}'_{1d} \cdot \mathbf{u}'_g}$). The mean power input cannot be affected because the longterm time average of $\overline{\boldsymbol{\tau}_{1d}}$ and $\overline{\mathbf{u}_g}$ will still contain all the necessary information from every timestep of the model. We can assess how much this impacts our estimates by using one day averages of surface velocity to reconstruct the equivalent calculation for the full surface velocity. For JRA55IAF and JRA55ABS, using one day averages to calculate the wind power input reduces the total by $\sim$ 17%. In the case of CORE2NYF the reduction is only $\sim$ 10%. The reduced impact is likely because of the lower frequency of the forcing, which means that there are fewer frequencies that get averaged away than for the JRA55-do-forced experiments. This suggests that the geostrophic estimate of eddy power input may be underestimated in magnitude by $\sim$ 10–20%. However, some of the decrease is probably due to inertial and near-inertial motions being filtered from the surface velocity by the daily averaging. As such, we expect 10% to be an upper bound on the error in the model's geostrophic power input estimates.

There is a strong seasonal cycle in Southern Ocean wind and surface wind stress in reanalyses (Hogg et al., 2015; Lin et al., 2018). We also find a seasonal cycle in KE and geostrophic KE in all three models (see Section 5). As such, we would expect to find a seasonal cycle in the total power input from the wind and in its Reynolds' averaged components. To investigate we construct seasonal averages from daily values of wind stress and SSH over the three month periods January–March (JFM), April–June (AMJ), June–September (JAS) and October–December (OND) for the period 2003–2007. We redefine the mean wind stress and SSH on a seasonal basis such that both the mean and eddy power input components may contain sub-annual variability.

In the seasonal averages of Fig. 4, JRA55IAF and JRA55ABS show the same broad patterns as in the full averages of Fig. 3c and f. For JRA55IAF the damping due to relative wind stress visually dominates with large amplitude values in areas of expected high EKE. Shallow seas are dominated by power input in all seasons. JRA55ABS shows the familiar pattern of inter-mingled positive and negative region at small scales. The highest amplitudes are still found around the ACC band, where EKE is expected to be higher. There is a general pattern of higher amplitudes for both models in the AMJ and JAS averages, i.e. the austral autumn and winter. This is borne out by the area integrals of Table 3. Both models show higher total geostrophic power input in AMJ and JAS. The maximum (and average, not shown) zonal wind stress is also higher for these two seasonal averages, as expected. This higher wind stress contributes to the mean power input of both models also being higher in AMJ and JAS.

The integrated eddy power input for JRA55IAF is negative in every season, whilst that of JRA55ABS is positive. However, whilst JRA55ABS has the expected pattern of higher eddy power input in AMJ and JAS, JRA55IAF's eddy power input is less negative in AMJ and JAS than it is in JFM and OND. This is contrary to our expectation that stronger wind should lead to more damping, especially in AMJ when the overall power loss is about half of that in JFM and OND. We can reconcile this by splitting the integral into regions where the eddy power input is positive and negative. As per Table 3, we can then see that for both models the gross power loss is higher in austral winter. However, the gross power gain is also higher in the same period. For JRA55IAF the increase in gross power gain is proportionally higher than for the gross power loss, leading to a net decrease in the integrated eddy power input. In contrast, the gross power gain and loss for JRA55ABS both increase in magnitude by about the same proportional amount. Hence, the integrated eddy power input also increases by about the same proportion.

5. Eddy kinetic energy

Kinetic energy responds quickly to the change in forcing between CORE2NYF and JRA55IAF, as well as to the transition to absolute wind stress in JRA55ABS. This is illustrated in the timeseries of Fig. 5a, which is built from squared daily means of surface velocity, for comparison with Fig. 5b. Note that the use of squared daily mean velocity, as opposed to daily mean of squared velocity, underestimates the KE by $\sim$ 20%. JRA55IAF has a higher minimum value than CORE2NYF over the seasonal cycle, and yet the maximum value is about the same, and there is not a particularly notable spinup period at the beginning of JRA55IAF. However, there is more interannual variability in the seasonal cycle in JRA55IAF, as might be expected due to the normal year forcing in CORE2NYF. After the change to absolute wind stress in JRA55ABS there is a 2–3 year transition period in which the kinetic energy grows by $\sim$ 25%. This time scale is fairly typical of the eddy field's response to a change in wind stress (see, e.g., Meredith and Hogg, 2006). The timeseries of geostrophic KE in Fig. 5b, constructed using daily averages of SSH, shows a similar pattern albeit with a seasonal cycle of lesser magnitude. Some of this magnitude reduction will be due to the loss of high frequency SSH variations from using daily mean values to calculate geostrophic KE. However, it still suggests a

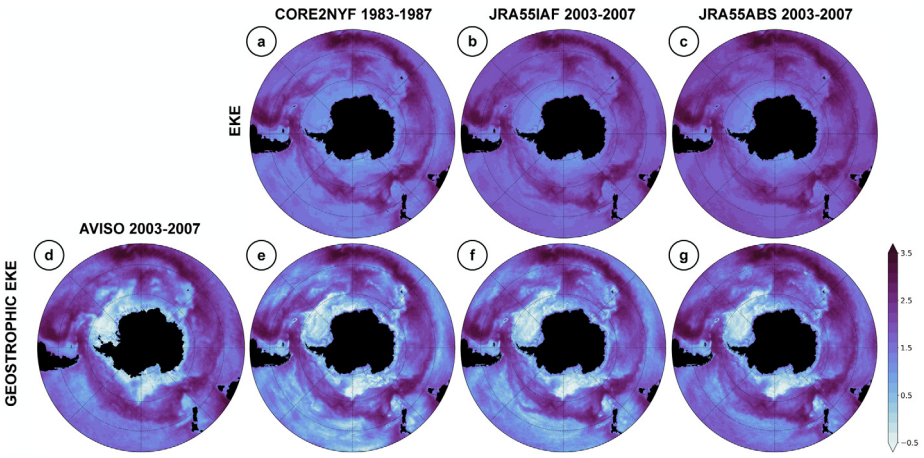

Fig. 6. Logarithm of surface eddy kinetic energy (top row), obtained via Reynolds averaging velocity squared, and logarithm of geostrophic surface eddy kinetic energy (bottom row), obtained from Reynolds averaging geostrophic velocities via Eq. (4), in $cm^2\ s^{-1}$. Data sources and time periods are as shown in the panel captions. (a,b,c) Total surface EKE for CORE2NYF, JRA55IAF and JRA55ABS, respectively. (d) Surface geostrophic EKE from AVISO, obtained by Reynolds averaging absolute geostrophic velocities. (e,f,g) Geostrophic EKE for CORE2NYF, JRA55IAF and JRA55ABS, respectively. Time averaging is over the calendar years 2003–2007 for all data sources. Solid black is land. Only the model domain south of 35°S is shown.

significant amount of surface variability is due to ageostrophic motions, such as inertial oscillations and Ekman affects.

The spatial variation of the EKE is shown in Fig. 6 as a series of five year averages for both total and geostrophic EKE. For JRA55IAF and JRA55ABS we average over the period 2003–2007 and use the last five years of the run (1983–1987) for CORE2NYF. We also include an estimate of observed geostrophic EKE from AVISO altimetry, which can be more directly compared with geostrophic EKE than the total EKE. The patterns are typical of that found in models of similar resolution, e.g. Barnier et al. (2006), Delworth et al. (2012) or Penduff et al. (2010). High values are seen in the core of the ACC, within the separated Agulhas Current, where the Brazil and Falklands currents meet and near bathymetry, such as Kerguelen Island/Plateau. Away from these regions the EKE is lower, although there is a general increase from CORE2NYF to JRA55IAF to JRA55ABS, which is consistent with the timeseries of Fig. 5. The regions of high EKE are particularly prominent in the geostrophic EKE panels due to very low values in the seasonal ice zone, which is also seen in the AVISO estimate. The geostrophic EKE of CORE2NYF and JRA55IAF are consistently lower than AVISO to the north of the ACC. The general increase in EKE for JRA55ABS leads to a better comparison in this respect.

The zonal average of Fig. 7a indicates that, on average, the total EKE of JRA55ABS exceeds that of the other models at every latitude. North of the Agulhas Current, between roughly 40°S and 30°S, JRA55ABS is a good fit to the AVISO estimate. South of approximately 55°S, all three models have higher EKE in the zonal average than AVISO. In the range 55–40°S, CORE2NYF and JRA55IAF are roughly on par with AVISO whilst JRA55ABS exceeds it. The story is somewhat different for geostrophic EKE in Fig. 7b. All three models are roughly on par with AVISO south of 55°S, suggesting that the "extra" EKE in Fig. 7a is largely ageostrophic in nature. North of the Agulhas current, all three models are low in EKE. Whilst JRA55ABS is a good fit to EKE in the latitude band 55–40°S, the other two models are on par with each other and below the AVISO estimate. Overall, the EKE of the models is as good a match to observations as most other models of similar grid spacing.

Averaged over the whole domain, JRA55ABS has 50% more surface EKE than either of the other two models. For the total EKE, the surface average value for JRA55ABS is 0.018 $m^2\ s^{-1}$, compared with 0.012 $m^2\ s^{-1}$ for both CORE2NYF and JRA55IAF. The proportional increase for the geostrophic EKE is similar, with values of 0.014 $m^2\ s^{-1}$ for JRA55ABS and 0.009 $m^2\ s^{-1}$ for CORE2NYF and JRA55IAF. The $\sim$ 30 GW of power removed from the eddy field discussed in Section 4 appears small compared to the $\sim$ 0.5 TW supplied to the geostrophic flow. However, as it is applied directly to each individual eddy its removal is able to affect significant change in the eddy field. This increase in EKE between JRA55IAF and JRA55ABS is consistent with the results of Renault et al. (2016a,b, 2017, 2019), Seo et al. (2016)

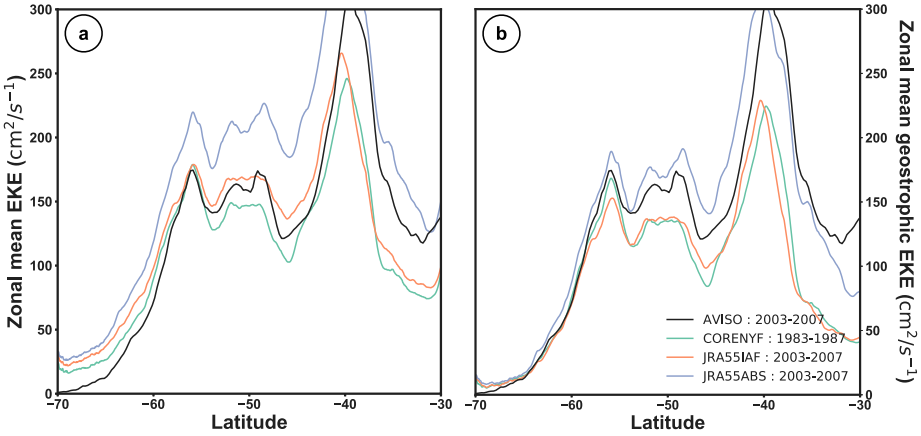

Fig. 7. Zonal average of (a) total surface eddy kinetic energy and (b) geostrophic surface eddy kinetic energy from Fig. 6. Both panels are in $cm^2\ s^{-1}$. The data sources and time periods are as shown in the legend to panel (b). The AVISO (black) line in each panel is the same.

and Seo (2017). These results suggest that this 50% increase in surface EKE is robust across most of the ocean's major current systems (the Bay of Bengal stands out with a particularly large change in EKE Seo et al., 2019). These results also include fully coupled models, where the increase in EKE between experiments such as JRA55IAF and JRA55ABS is moderated by an accompanying increase in the wind stress. This suggests that for a coupled model, the neglect of relative wind stress/ocean current interaction would lead to an ~ 35% increase in surface EKE (Renault et al., 2016b). Our analysis of both total EKE and geostrophic EKE implies that this increase would be largely in the geostrophic component of the flow, i.e. the most relevant to the general circulation of the ocean.

6. Heat transports and fluxes

At statistical equilibrium the ocean's stratification will no longer be adjusting to changes in forcing, when considering a long enough time average, and the divergence of the ocean heat transport must match the surface heat flux. After the 20–40 years of model integration our numerical experiments are not at statistical equilibrium. However, the mixed layer has adjusted and we might expect that the surface heat fluxes are close to their final value. The subsurface density structure is still adjusting, which means that individual density layers may be gaining or losing volume, and care must be taken when interpreting the ocean heat transport. However, a decomposition of the heat transport can be used to indicate an important route through which the changes in the eddy field outlined in Sections Section 5 (and Appendix B) can affect global climate.

We estimate the model's heat transport (note this is a misleading choice of nomenclature, albeit consistent with the extant literature, see Warren, 1999) using time-averages of the product of the meridional velocity (v), the potential temperature (T) and the vertical grid spacing at v-points (e_{3v}). This takes account of the evolution of all the quantities at every timestep, as well as ensuring that the MUSCL advection scheme is properly accounted for. The temperature transport is then Reynolds' averaged thusly

$$\rho_0 c_p L_x \int_{-H}^{\eta} \left\langle \overline{vT} \right\rangle \mathrm{d}z = \rho_0 c_p L_x \int_{-H}^{\eta} \langle \overline{v} \rangle \left\langle \overline{T} \right\rangle \mathrm{d}z + \rho_0 c_p L_x \int_{-H}^{\eta} \left\langle \overline{v}^* \overline{T}^* \right\rangle \mathrm{d}z + \rho_0 c_p L_x \int_{-H}^{\eta} \left\langle \overline{v'T'} \right\rangle \mathrm{d}z, \quad (5)$$

where $\rho_0 = 1026$ kg m^{-3} is the Boussinesq reference density, $c_p = 3991.9$ J kg^{-1} K^{-1} is the specific heat capacity, L_x is the zonal extent of the ocean (as a function of latitude), $-H$ is the depth of the sea bed, η is the height of the free surface, $\bar{\bullet}$ indicates a time averages, $\bullet'$ indicates the deviation from the time average, $\langle \bullet \rangle$ indicates a zonal average and $\bullet^*$ indicates deviations from the zonal mean. We take the time average over the five year period 2003–2007, the same time period used for our analysis of EKE (and temperature variance in Appendix B) for JRA55IAF and JRA55ABS.

The first term on the right-hand side of Eq. (5) is the mean heat transport and largely reflects the Eulerian overturning. The second term on the right-hand side is the heat transport due to standing meanders, i.e. all deviations from a strictly zonal flow in the time mean. The third term on the right-hand side is the contribution of purely transient features crossing lines of constant latitude. If the zonal integration was replaced with an integration following the flow, then the standing component would become very small and be replaced by a larger transient component (Marshall et al., 1993).

The thick green line in Fig. 8a is the total heat transport for experiment JRA55IAF, whilst the thin line is the same for JRA55ABS. The total heat transport has previously been found to be largely insensitive to model formulation and resolution (Meijers et al., 2007, and references therein). The structure and form of the total heat transport for both models is broadly consistent with that of previous estimates, such as those of Meijers et al. (2007) and Mazloff et al. (2010). The

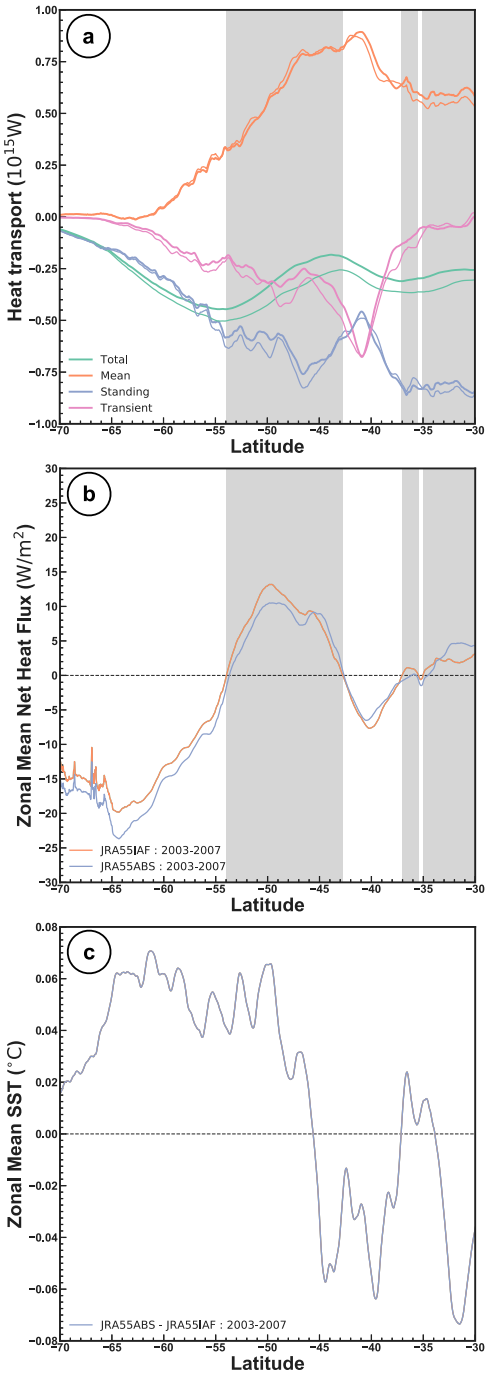

Fig. 8. (a) Reynolds averaged meridional heat transport in PW for JRA55IAF (thick lines) and JRA55ABS (thin lines) over 2003–2007. (b) Zonally-averaged net heat flux in W m^{-2} for JRA55IAF and JRA55ABS over 2003–2007. Grey shading marks where the net heat flux changes sign in JRA55IAF. (c) Zonally-averaged SST difference between JRA55ABS and JRA55IAF in °C.

total heat transport of JRA55ABS is higher in magnitude than that of JRA55IAF at every latitude, although it tends to have its maxima and minima at roughly the same latitudes (indicating that the ocean heat transport is converging/diverging heat in roughly the same latitude bands).

The decomposition of Eq. (5) allows us to attribute the difference in total heat transport between the two experiments to mean or eddy transport processes. As shown by the thick and thin orange lines in Fig. 8a, there is little substantial differences between the mean heat transport of each model. Given the relatively minor change in zonal

wind (a 1% change in the maximum and 2.7% change in the mean) and short integration time, it is unsurprising that there is little difference in mean heat transport. The change in wind would not be expected to cause a major shift in the flow structure and any changes in temperature transport have not been active for sufficiently long to influence the mean stratification. If the model was given longer to spinup, then the mean stratification might change enough to allow the mean flow to transport more/less heat by altering the top-to-bottom temperature difference at each meridional location.

With the mean heat transport undergoing little change, it stands to reason that the difference in total heat transport between JRA55IAF and JRA55ABS must be due to standing and/or transient meaders. This is borne out by the pairs of blue and fuchsia lines in Fig. 8. It is generally the case that the magnitude of JRA55ABS's standing and transient heat transport are higher than those of JRA55IAF. At most latitudes, both contribute to making the total heat transport more southwards in JRA55ABS. The generally southwards heat transport of these components is consistent with previous model estimates, e.g. Jayne and Marotzke (2002), Meijers et al. (2007) and Mazloff et al. (2010), as well as many observational estimates from, e.g. floats (Gille, 2003; Sallée et al., 2008) or satellites (Stammer, 1998; Hausmann and Czaja, 2012). Observational estimates of eddy heat transport are consistently southwards with error bars that are a large enough, relative to the estimates, so as to overlap and make them indistinguishable.

The differences in transient heat flux are consistent with the general increase in EKE from JRA55IAF to JRA55ABS, since $\sqrt{2EKE}$ is a good estimate of the velocity anomaly v' in $\overline{v'T'}$. Similarly, $\sqrt{\overline{T'T'}}$ would be a good estimate of the temperature anomaly in $\overline{v'T'}$. As such, the lack of substantial change in temperature variance (seen in Appendix B) indicates that the eddy heat transport is largely altered by changes in the rate at which transient/standing features move warmer/colder water around, rather than a change in temperature of the water being moved.

The grey shading in Fig. 8a indicates where the zonally averaged net surface heat flux changes sign, as shown in Fig. 8b. For both JRA55IAF and JRA55ABS we find this is at similar latitudes. By comparison, it can be seen that in regions where there is stronger heat convergence in JRA55ABS, largely driven by changes in eddy fluxes as described above, there is more heat lost by the ocean. For example, between 54°S and the pole, the ocean heat transport in each model is converging and so the zonal mean net heat flux is negative (upwards), indicated a loss of heat to the "atmosphere". Because the heat transport at 54°S is stronger in JRA55ABS, more heat is converging into this region than in JRA55IAF, and so the zonal mean net heat flux is larger in magnitude. In contrast, between 43°S and 54°S the heat transport in both models is divergent, and so they are gaining heat at the surface. However, as the heat transport difference is a near constant offset between the models, there is little difference in the net heat flux even though the magnitude of the heat transport in JRA55ABS is higher.

The change from relative to absolute wind also affects the other air–sea fluxes calculated by the bulk formulae. Due to this, it could be the case that the changes in heat flux in Fig. 8b are due to this modification, rather than the changes in the eddy field. The increased heat transport in Fig. 8a would then be the response of the ocean to balance this extra loss/gain of heat. Essentially, the causality would point in the other direction to that argued above. If we examine the zonal mean SST difference in Fig. 8c, we find that, south of $\sim 45°$S, JRA55ABS has warmed relative to JRA55IAF. This indicates that it is the change to absolute wind elevating the EKE that drives the change. The elevated EKE then increases the eddy heat transport, resulting in warmer SST and increased net heat loss. If the net heat flux led the change, we might instead expect to see a decrease in SST, which would be partially compensated by the increased heat transport.

The increased convergence of heat between 54°S and the pole in JRA55ABS could potentially alter the seasonal cycle and/or mean ice cover in this region. Due to the strong link between planetary albedo and climate, this is a route for the change from relative to absolute wind stress to have global reach. To establish such a link, we examine the difference in sea ice between the two models in .

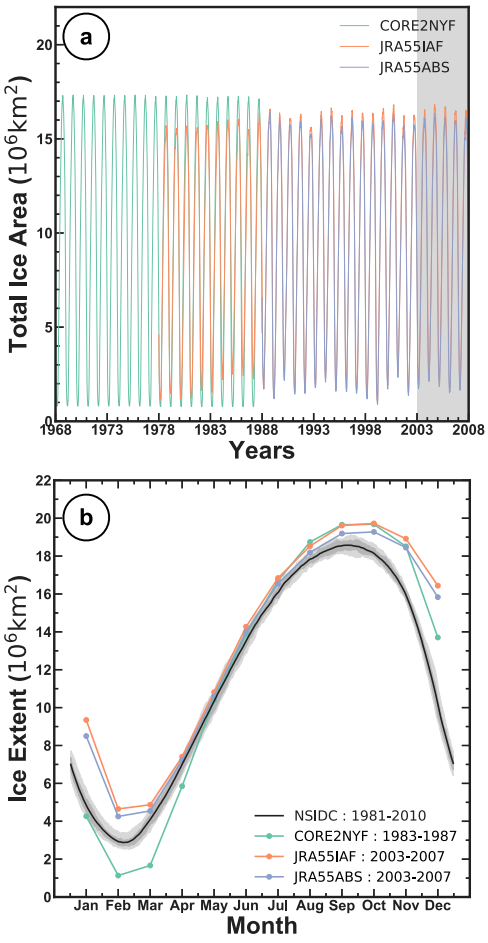

Fig. 9. (a) Time series of ice area built using daily means of ice concentration for CORE2NYF, JRA55IAFand JRA55ABS. The grey shading highlights the time-averaging period used for JRA55IAF and JRA55ABS for previous/subsequent figures. (b) Daily values of ice extent from the NSIDC sea ice index (black line) with interquartile (dark) and interdecile (light) range shaded. Colours, as per legend, are monthly averages from the three NEMO experiments.

7. Sea ice extent and seasonal cycle

The seasonal cycle in total sea ice area for CORE2NYF is very regular, as shown by the green line in Fig. 9a. This is consistent with the more regular, with respect to JRA55IAF and JRA55ABS, seasonal cycles in other quantities, such as kinetic energy (see Fig. 5a). The transition to the JRA55-do forcing set introduces interannual variability in the total ice area, as well as contracting the range of minimum-to-maximum ice area (orange and mauve lines in Fig. 9a). The use of absolute wind stress acts to reduce the minimum and maximum total ice area slightly.

We compare the model sea ice cover with satellite derived data from the National Snow and Ice Data Center's (NSIDC) sea ice index (Fetterer et al., 2017, updated daily) and monthly averages of sea ice concentration (Cavalieri et al., 1996, updated yearly). We begin with the NSIDC's ice extent, which assumes total ice cover wherever sea ice concentration > 0.15. We compare a five year climatology of monthly values for each model experiment to the NSIDC Antarctic sea ice extent from 1983–2010. We use pentades of 1983–1987 for CORE2NYF and 2003–2007 for JRA55IAF and JRA55ABS to correspond with previous

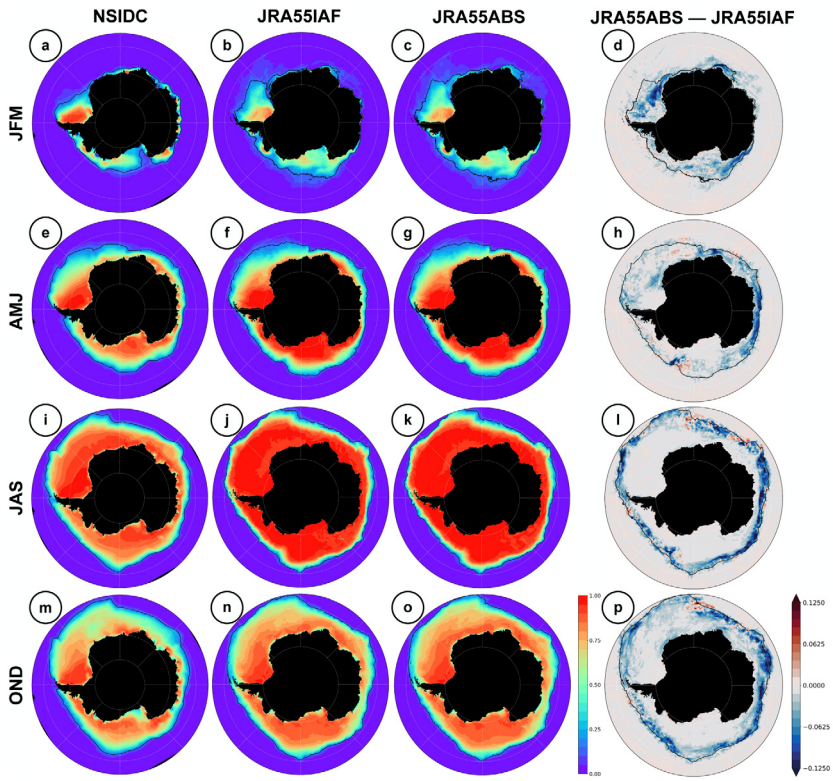

Fig. 10. Seasonal sea-ice concentration arranged by column for data source (left to right; NSIDC, JRA55IAF, JRA55ABS and JRA55ABS minus JRA55IAF) and by row for season (summer, autumn, winter, spring). Solid black is land. Only the domain south of 55°S is shown. Black contour is the 15% sea ice concentration line for the data source in panels a–c, e–g, i–k and m–o. For panels d, h, l and p it is the 15% sea ice concentration line for JRA55IAF.

analysis. In Fig. 9b we also include the NSIDC interquartile and inter-decile ranges as dark and light grey shading, respectively. The NSIDC data are plotted as average daily values, in contrast to the monthly averages for the model data.

The sea ice extent of JRA55IAF and JRA55ABS is greater than that of the NSIDC record over the entire year. It is plausible that the extra freshwater, added to prevent polynya formation, may contribute to this extra sea ice. However, it is not possible to definitively conclude this without an additional, costly, numerical experiment. Over the ice growth season of April to August, JRA55IAF and JRA55ABS remain a roughly constant offset of $\sim +1\times10^6$ km^2 from the NSIDC data, implying that their growth rates are a good match. During September to March, JRA55IAF and JRA55ABS ice extent exceeds that of the NSIDC data by a larger amount. Throughout the year, JRA55ABS ice extent is less than that of JRA55IAF. This is consistent with the ice area timeseries of Fig. 9a and, whilst the difference is small, it is present throughout the year over the full length of JRA55ABS. In contrast to JRA55IAF and JRA55ABS, CORE2NYF's ice extent is much lower than the NSIDC data in February and March. It grows very rapidly from April to August, such that it exceeds the ice extent of the NSIDC data over the winter, before melting very rapidly in December and January.

A more detailed breakdown of seasonal ice concentrations is presented in Fig. 10, which uses NSIDC seasonal data in concert with pentadal averages of JRA55IAF and JRA55ABS over the same three month periods. The spatial maps of seasonal average ice concentration reinforce the clear pattern of ice growth and melt in Fig. 9. The JFM average broadly corresponds to the period of ice extent minimum with peak ice extent occurring in the final month of the JAS average. The AMJ and OND seasonal averages are periods of rapid sea ice growth and melt, respectively. We concentrate on JRA55IAF and JRA55ABS, which have more realistic ice extent/concentrations than CORE2NYF, to develop the previous Section's argument regarding the impact of relative vs. absolute wind stress on heat transport.

In terms of the general spatial pattern, there is a good agreement between the JRA-forced NEMO models and the NSIDC seasonal data. In JFM, high concentrations are restricted to a small region of the western Weddell Sea and the Ross Sea. Whilst the ice extent of JRA55IAF and JRA55ABS is systematically higher than that of the NSIDC, in this season we find that ice concentrations are lower, but spread over a broader area.

Over the growing season, and towards the peak sea ice extent in September, the ice concentrations for JRA55IAF and JRA55ABS are broadly similar. The regions of ice concentration > 0.8 expand rapidly over AMJ (Figs. 10f,g) and over the JAS season the characteristic pentagon with near total ice coverage is achieved. Notably, the models have higher concentrations over large areas, in contrast to the NSIDC seasonal averages in Fig. 10e and i. The satellite observations tend towards a concentration of 1 in similar regions that retain high concentration in JFM (Fig. 10a). However, the typical concentration is around 0.75, rather than the ~ 1 of the NEMO models. This does not impact the sea ice extent comparison in Fig. 9 because the satellite observations and models both have large areas with sea ice concentration > 0.15. Over the course of the OND averaging period, the sea ice melts and the sea ice edge retreats towards the Antarctic continent. There is not a big discrepancy between the NSIDC (Fig. 10m) and JRA55IAF/JRA55ABS(Fig. 10n–o). The model OND seasonal averages do tend towards more complete coverage, as in the JAS average. In addition, the regions that retain high ice concentration, or broader coverage at lower concentration, than NSIDC, in JFM also tend to high concentration in this season.

Taking the difference between the JRA55IAF and JRA55ABS shows where the use of relative wind stress acts to increase ice cover, as per Fig. 10d, h, l and p, for the four seasons. Across the four seasons we find that absolute wind acts to decrease sea ice concentration in a broad circumpolar way. The largest differences are at the edge of the ice pack and there are only very small areas where absolute wind stress increases sea ice cover. The decrease in sea ice is not concentrated at specific

bathymetric features, such as Kerguelen Plateau or the Southeast Indian Ridge. This indicates that if the increased eddy heat transport under absolute wind stress does take preferred routes in localised regions the additional heat is spread throughout the Southern Ocean by the rest of the circulation. It is in JAS and OND, when the ice extent is large and ice concentration is typically > 75% that the extra sea ice in JRA55IAF, with respect to JRA55ABS, is most concentrated. In JFM and AMJ, the extra sea ice is more diffusely spread out, particularly in the Weddell Sea. This may reflect the local circulation redistributing ice concentrations as the ice pack breaks up/forms.

In summary, we note that the ice extent and ice area for JRA55ABS is always lower than that of JRA55IAF. The difference is relatively small, but systematic, and does not appear to be tied to a specific region of the Southern Ocean. The reduced ice cover of JRA55ABS is consistent with the larger convergence of heat into the seasonal ice zone seen in Section 6. Not only does this lead to higher SST and higher net heat loss, the additional heat acts to reduce sea ice cover in all seasons.

8. Summary and discussion

Relative wind stress acts as a form of friction at the sea surface that torques down every single eddy (Dewar and Flierl, 1987) and equatorial wave (Pacanowski, 1987). In our model, this leads to a loss of power $\sim$ 30 GW from the geostrophic eddy field, once the high power input areas on the shelf are ignored. This power sink is small, but has a disproportionate impact upon the surface EKE leading to an $\sim$ 50% increase under absolute wind stress, which is consistent with other major current systems (Renault et al., 2016a,b, 2017, 2019; Seo et al., 2016; Seo, 2017; Seo et al., 2019). This impacts the heat transport of the eddy field such that under absolute wind stress the polewards heat transport is increased in magnitude at all latitudes. Due to the meridional structure, there is then a stronger convergence of heat into the seasonal ice zone, which is accompanied by higher SST, greater heat loss to the atmosphere and reduced ice cover throughout the year.

The surface wind stress is a transfer of momentum between atmosphere and ocean. In a coupled model, the reduction in ocean currents due to relative wind stress reduces the momentum transfer from the atmosphere. Relative to an equivalent ocean-only experiment, this leads to a slightly stronger wind stress (although still less than an absolute wind case). This increased wind stress then leads to a partial re-energisation of the ocean EKE, with respect to the same ocean-only experiment. The result being that in a coupled system the EKE difference between absolute and relative wind experiments is lower than found here, at about 35% (e.g. Renault et al., 2016b). We would therefore expect the impact on the heat transport, and the ice cover, to similarly be ameliorated. However, we would also expect the coupled system to less vigorously damp the SST anomalies associated with long-lived mesoscale features (see Appendix B). This may partly offset the amelioration of the EKE change and offset any impact on the meridional heat transport. However, we do not see a significant impact of absolute vs. relative wind stress on the temperature variance/air–sea heat flux feedback and so it is difficult to speculate how these would be impacted in a coupled model with certainty. Note that the impact of ocean velocity acts on every aspect of the bulk formulae where it would normally apply, not just the wind stress calculation, and so even a coupled model's heat fluxes, etc., would experience both direct and indirect impacts from relative wind stress.

A remaining question is how differing resolution in coupled models impact the difference between relative and absolute wind stress. For example, if the wind stress is calculated on the atmospheric grid, which is significantly coarser than the ocean one, how much does this influence the damping due to relative wind stress? Would we see the same increase in EKE/polewards ocean heat transport as under absolute wind stress seen here? How different resolutions of coupled model, both atmosphere and ocean components, might impact the strength of air–sea heat flux feedbacks is also currently unknown.

The total heat transport in a coupled model is largely fixed, primarily set by the geometry of the planet in question and the amount of in-coming solar radiation (Stone, 1978). We would therefore expect a coupled model to compensate the changes in the ocean by reducing the heat transport in its atmosphere. In idealised coupled models, relatively minor seeming changes in the heat transport partitioning can lead to large changes in global climate (Marshall et al., 2007; Ferreira et al., 2010, 2011). As a result, even if the reduction in planetary albedo, due to reduced ice cover, under absolute wind stress did not lead to significantly more absorbed solar radiation, such a repartitioning may be a route to affect global climate.

CRediT authorship contribution statement

David R. Munday: Conceptualization, Methodology, Investigation, Data curation, Writing – original draft, Writing – review & editing. **Xiaoming Zhai:** Conceptualization, Methodology, Writing – original draft, Writing – review & editing. **James Harle:** Software, Data curation, Writing – original draft. **Andrew C. Coward:** Software, Supervision. **A.J. George Nurser:** Writing – original draft, Writing – review & editing, Supervision, Project administration.

Declaration of competing interest

The authors declare that they have no known competing financial interests or personal relationships that could have appeared to influence the work reported in this paper.

Data availability

NEMO is available from https://www.nemo-ocean.eu. The details of the model configuration used here are available from https://doi.org/10.5281/zenodo.4707331. The model data for CORE2NYF(http://dx.doi.org/10.5285/2e982e6692e3427dbe35e64ad9dee12d),JRA55IAF (https://catalogue.ceda.ac.uk/uuid/67ad0c489e2b4d18aa152e78f28ae0c0)and JRA55ABS (https://catalogue.ceda.ac.uk/uuid/aa4106a7a35246dfb84fb925a7d65650)are available from the British Oceanographic Data Centre (BODC) at the embedded links. ECCOv4r2 can be obtained from https://dataverse.harvard.edu/dataverse/ECCOv4r2. The Ssalto/Duacs altimeter (AVISO) products were produced and distributed by the Copernicus Marine and Environment Monitoring Service (CMEMS) (https://marine.copernicus.eu). The ESA Climate Change Initiative SST data can be accessed from http://www.esa-sst-cci.org/PUG/pug.htm. The Southern Ocean State Estimate data are available from http://sose.ucsd.edu. The Community Earth System Model data are available at https://www.earthsystemgrid.org/dataset/ucar.cgd.asd.cs.hybrid_v5_rel04_BC5_ne120_t12_pop62.ocn.proc.daily_ave.html. The Climate Forecast Reanalysis data are distributed by the National Climatic Data Center of NOAA at https://rda.ucar.edu/datasets/ds093.2. The National Sea and Ice Data Center Sea Ice Index and monthly images can be obtained from https://nsidc.org/data.

Acknowledgements

This work was supported by the Natural Environment Research Council [ORCHESTRA, Grant Number NE/N018095/1]. This work used the ARCHER UK National Supercomputing Service (http://www.archer.ac.uk) and JASMIN, the UK collaborative data analysis facility. DRM thanks Pierre Mathiot for early help with the NEMO configuration, Emma Young for many discussions on NEMO setup and model verification, Chris Bull for help with python, ocean forcing sets and github, and Kaitlin Naughten for interesting discussions about Weddell Sea polynyas.

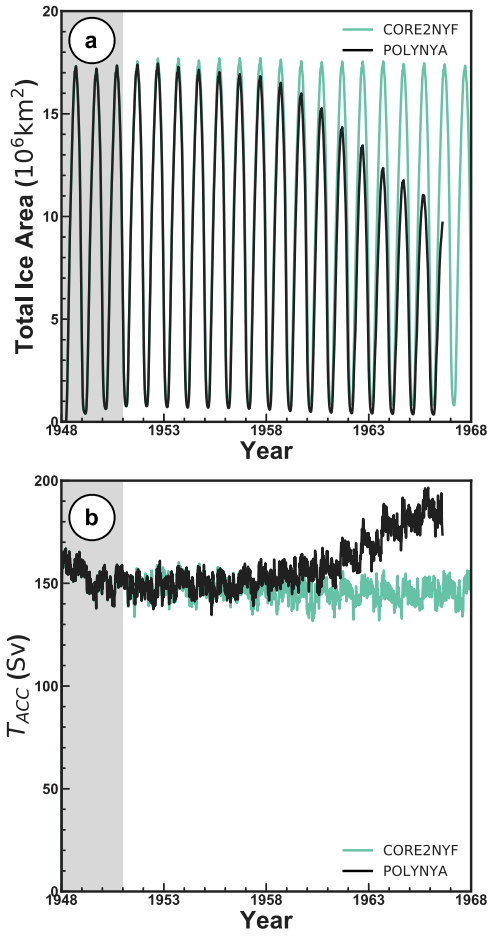

Fig. A.1. (a) Timeseries of total ice area over the first 20 years of the CORE2NYF control run and the initial POLYNYA test run. The time series is from daily mean ice concentrations. (b) Timeseries of Drake Passage transport over the first 20 years of the CORE2NYFcontrol run and POLYNYA from 5-day means of the zonal velocity. In both panels, grey shading shows the initial spinup period in which the temperature/salinity are reset to ECCOv4 at the end of each year.

Appendix A. Weddell sea polynya formation

In this Appendix we take a brief look at the development of the Weddell Sea polynya found in initial tests and suppressed by the addition of extra freshwater. We identify the CORE2 normal year forced run that produced the Weddell Sea polynya as POLYNYA. This description is intended to illustrate the development of the polynya allowing it to be traced backwards in time to its initiation.

In Fig. A.1a the black line shows the evolution of the total ice area for POLYNYA over the full-length of its model run, juxtaposed with the first 20 years of CORE2NYF's total ice area. The seasonal cycle of CORE2NYF is very regular; there is little interannual variation in either the maximum or minimum ice area. This remains true over the full 40 years of the CORE2NYF control. In contrast, POLYNYA's maximum ice area is markedly reduced by the end of its tenth year (nominally 1957) and the decrease subsequently becomes precipitous. By the winter of 1966, POLYNYA's maximum ice area is under 60% of CORE2NYF's at the same point in time (ice thickness is also about 60% of CORE2NYF, with the volume being about 56%). Shortly before reaching the expected peak ice concentration in 1966, POLYNYA becomes numerically unstable and the model run comes to an abrupt end. This numerical instability is caused by an increasing density difference across the model's ACC, which leads to a $\sim 25\%$ increase in the Drake Passage transport over the second half of POLYNYA, as shown in Fig. A.1b.

POLYNYA's issues begin in the central Weddell Sea as a thinning of the sea ice that results in an open polynya in winter (see Fig. A.2a). The polynya consistently reopens in the western Weddell Sea whilst extending eastwards towards Maud Rise. As shown in Fig. A.2b, the polynya also extends northwards until it reaches the ice edge, at which point it resembles a bite taken out of the ice, rather than a polynya. Compared to the 1965 ice cover of CORE2NYF in Fig. A.2c, the reduction in ice area/extent is clear.

The development of the polynya can be traced backwards in time via the model's surface age tracer. As described in Section 2, this ideal age tracer is set to zero within 10 m of the surface and 2° of the northern boundary. Low age at depth, i.e. dark blue in Fig. A.3, indicates that water has been recently ventilated via contact with the surface through deep convection. As is typical with models that produce Weddell Sea polynyas, deep convection occurs throughout the water column in POLYNYA. When the model run experiences numerical instability, this convection is over a large fraction of the Weddell Sea and is able to bring warm Circumpolar Deep Water (CDW) to the surface and melt large amounts of the seasonal sea ice (Fig. A.3b). By looking back through earlier years, we are able to track the evolution of the deep convection and the polynya. As shown in Fig. A.3a, five years previous to the numerical instability the deep convection is at the northern edge of the continental slope. In fact, the convection originates over the shelf and marches out over the continental shelf as each winter season occurs. This is due to the successive years of winter cooling weakening the near surface stratification, which allows the next year's heat loss to generate convection slightly further out from the coast. The polynya only forms when the edge of the convection reaches the warm CDW and brings sufficient heat to the surface so as to melt any sea ice. In contrast, Fig. A.3c shows that in CORE2NYF convection never reaches the edge of the continental slope and is always confined to the top few hundred metres. The additional freshwater prevents surface water from becoming dense enough to reach the bottom of the Weddell Sea and so the warm CDW remains isolated from the surface.

Appendix B. Temperature variance and air–sea heat flux feedbacks

In addition to EKE, another measure of eddy activity is the temperature variance, which is a partial measure of eddy potential energy and links to Section 6's discussion of meridional heat transport. A full measure of eddy potential energy would examine density variance and/or include salinity variance. However, anecdotally, we find salinity variance to be very low in each of the models and choose to neglect it here. In this Appendix, we discuss how the temperature variance varies across our model experiments and use covariance of sea surface temperature (SST) and net surface heat flux to discuss how this might be related to air–sea flux feedbacks. We use a number of data sources to construct estimates of Sea Surface Temperature (SST) variance and the covariance of SST with net surface heat flux. We rely upon a range of other data sources available as high resolution gridded products.

As an observational record of SST and its variance we use v2.1 of the Level 4 Analysis Climate Data Record (CDR) from the European Space Agency's climate change initiative (ESA cci, Merchant et al., 2019; Good et al., 2019). These data are a globally-complete daily analysis of SST on a 0.05° grid and combine data from the Advanced Very High Resolution Radiometer (AVHRR) and Along Track Scanning Radiometer (ATSR) satellites. Where there are gaps in the measurements, data assimilation is used to provide SST. We use data from 1/1/2003 to 31/12/2007, corresponding to the analysis period of JRA55IAF and JRA55ABS, rather than the full length of the ESA cci record.

As an optimal combination of observations and model, we also make use of the Southern Ocean State Estimate (SOSE, Mazloff et al., 2010). SOSE uses a 1/6° ocean model and the adjoint method to construct a continuous trajectory through the model's phase space that is an optimal fit to many thousands of observations in a least-squares sense.

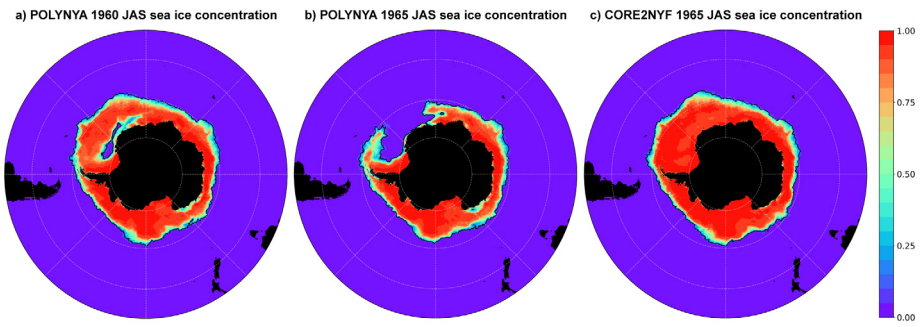

Fig. A.2. July–August–September average sea ice concentration for (a) POLYNYA in 1959, (b) POLYNYA in 1965, (c) CORE2NYF in 1965. The black line is the 0.15 sea ice concentration contour. Solid black is land. Only the model domain south of 35°S is shown.

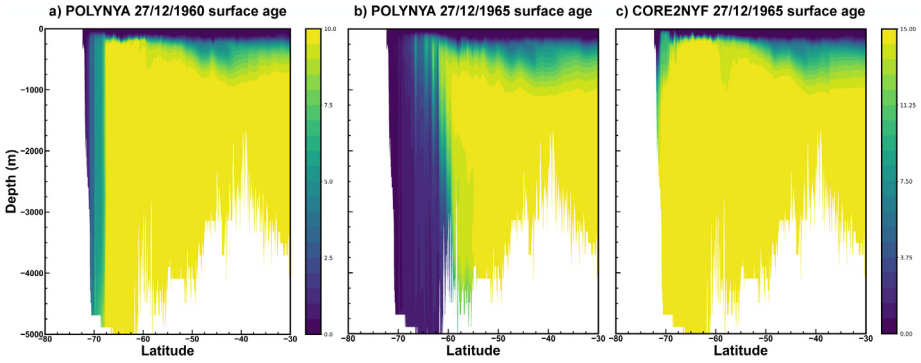

Fig. A.3. (a) Surface age tracer in years for POLYNYA from a five day mean beginning on 27/12/1969, (b) surface age tracer in years for POLYNYA from a five day mean beginning on 27/12/1969, (c) surface age tracer in years for CORE2NYF from a five day mean beginning on 27/12/1969. Note the change in colour bar between (a) and (b) & (c). Yellow is water as old as it can be, based on the length of the model run and the data given.

The initial conditions and surface forcing fields are subject to adjoint-based modification to facilitate the optimal fit. SOSE spans calendar years 2005–2010, although we discard the first year as model spinup.

Net surface heat flux observations are sparse over the Southern Ocean. As a result, when considering the covariance of SST and surface heat flux we use the NCEP Climate Forecast System Reanalysis (CFSR, Saha et al., 2010a,b) as a proxy for a purely observational data set. CFSR is a next generation reanalysis using global, high resolution, coupled atmosphere–ocean–sea ice–land surface components. The atmospheric component has a resolution of ~ 38 km (T382) with 64 levels and assimilates satellite radiances. It is coupled to a global ocean every 6 h. At the Equator, the ocean component has a grid spacing of $1/4°$, which extends to $1/2°$ outside of the tropics, and has 40 levels. CFSR spans calendar years 1979 to 2010 and we make use of the full reanalysis.

To provide a high resolution model estimate of SST variance and the covariance of SST and net heat flux, we use a version of the Community Earth System Model with a $1/10°$ ocean component (CESM, Small et al., 2014). This coupled model has an atmosphere with a $1/4°$ grid spacing and an ocean with a $1/10°$ grid spacing. This high resolution coupled model was run for a total of 100 model years, although we only use the last 5–15 years due to model spinup. The atmosphere communicates with the coupler every 10 min and the ocean communicates with the coupler every 6 h.

To compute SST variance we use daily mean values of SST from ESA cci, SOSE and CESM to construct 5 year time averages of SST and the square of SST. These are then Reynolds averaged to produce the variance of SST, $\overline{T'T'}$. For each NEMO experiment the square of SST is obtained directly from NEMO and so includes higher frequencies than the three comparators. This might be expected to elevate the $\overline{T'T'}$ of the NEMO experiments, although recalculation using a series of one day means of SST indicates a difference of $\lesssim 0.5\%$.

The spatial maps of surface temperature variance in Fig. B.1a–c show little qualitative difference between the three NEMO experiments, which broadly agree with the ESA cci estimate of Fig. B.1d. High values of temperature variance are found where the western boundary currents, i.e. the Brazil Current, Agulhas Current and East Australia Current, bring warm subtropical water southwards, potentially interacting with the ACC. The high values associated with the Agulhas Current persist for thousands of kilometres downstream of the Agulhas retroflection. There is a minimum in temperature variance within the core of the ACC, which is clearer and deeper in the NEMO experiments than in the ESA cci estimate. South of these minima, values are elevated in a roughly pentagonal shape characteristic of the winter sea ice edge. Very low values are then found close to Antarctica, where the temperature would be close to the freezing point for much of the year. In general, the ESA cci estimate has higher values of temperature variance than all three NEMO experiments throughout the model domain. This is particularly noticeable north of the ACC. For CORE2NYF there are notably higher variances in the Weddell and Ross gyres, with respect to JRA55IAF and JRA55IAF, which we attribute to the lower sea ice cover in summer allowing for more warming near the surface (see).

The temperature variance estimates from SOSE and CESM in Fig. B.1e and f show areas of much higher values than the NEMO models and ESA cci. The regions of higher temperature variance are located in similar geographical areas, such as east of the Kerguelen Plateau and south-east of New Zealand. The high variance at the edge of the seasonal ice zone stands out as being both broader in area and higher in value, although very low variance is still found at the heart of the Weddell and Ross Seas. The minimum in the core of the ACC is, however, still present. Because of the generally higher values, the minimum is obscured over much of the Atlantic and Indian sectors, with the most prominent region standing out between Drake Passage and New Zealand. However, as seen in the zonal average of B.2a, there is still a distinct minimum between 50°S and 60°S, which is visually

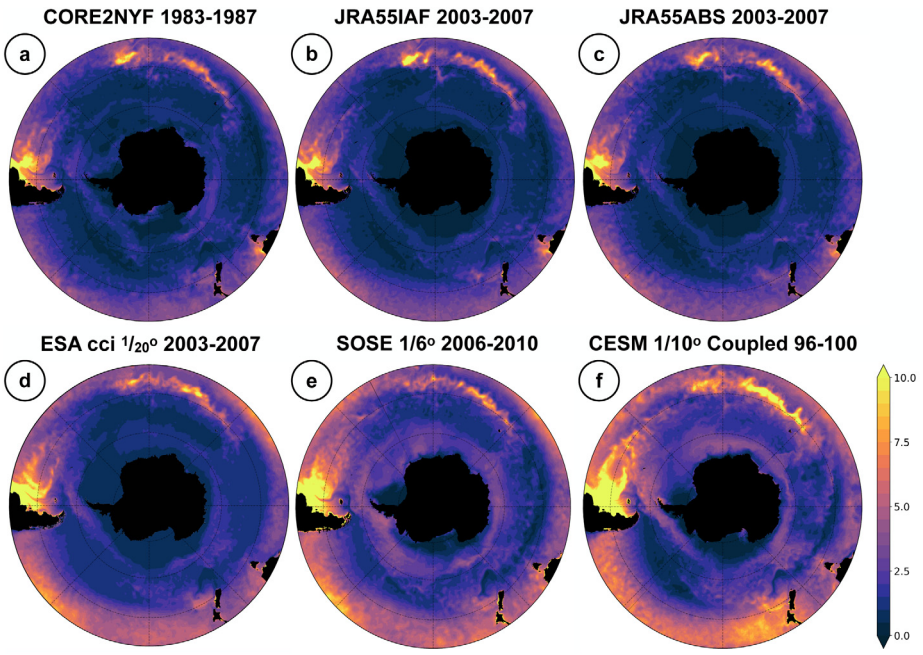

Fig. B.1. Surface temperature variance in K^2, obtained via Reynolds averaging temperature squared, for the data sources and time periods in the panel captions. (a,b,c) Temperature variance from the three NEMO experiments CORE2NYF, JRA55IAF and JRA55ABS, respectively. (d) An observational temperature variance from ESA cci. (e,f) Temperature variance estimates from SOSE, an eddy-permitting state estimate, and CESM, a coupled model with eddy-resolving ocean, respectively. The CESM estimate is from the last 5 years of its 100 year model run. Solid black is land. Only the domain south of 35°S is shown.

more prominent than in the other estimates due to the higher values to the south of 60°S. The zonal average also makes it clear that all three NEMO models have low temperature variance with respect to their comparators.

Why are all three NEMO models temperature variances systematically lower than the other estimates? It seems unlikely that it is a matter of model resolution; the grid spacing of SOSE is coarser than that of the CESM and NEMO configuration used here (the difference between the $1/10°$ of CESM and the $1/12°$ of our NEMO configuration is probably marginal). If the reason for the lower temperature variance in the NEMO experiments was a systematic under-representation of the ocean's eddy potential energy field, then it would be reasonable to expect SOSE to have lower variance than CESM and NEMO. It seems far more likely that some other systematic difference between the models is the reason for the variation in their temperature variance estimates.

The forcing sets for the NEMO experiments use a prescribed atmospheric temperature. In this sense, the atmospheric temperature is fixed and a key feedback between ocean and atmosphere is missing, since any heat flux anomalies due to SST anomalies cannot change the atmospheric temperature. In contrast, CESM is a coupled model and the presence of this feedback allows SST and atmospheric temperature to covary and influence each other's evolution through time. The lack of this feedback in ocean-only experiments is expected to result in overly-strong damping of the SST towards the atmospheric temperature imposed by the forcing set. As a result of this anomalies of SST are more rapidly eroded than would be the case in reality, or in a coupled climate model. SOSE is a six year long state estimate, although we have restricted our analysis to the last five years to allow for spinup of the forward model's eddy field. By adjusting its forcing and initial conditions, SOSE provides a dynamically consistent trajectory through phase space, which is an optimal fit to the contributing observations in a least-squares sense. In this regard, SOSE might be expected to give the optimal estimate of many of the ocean's properties, although it does so, in part, by adjusting the atmospheric temperature of its forcing. A side effect of this is to ensure that SST anomalies can persist in a similar manner to that of CESM.

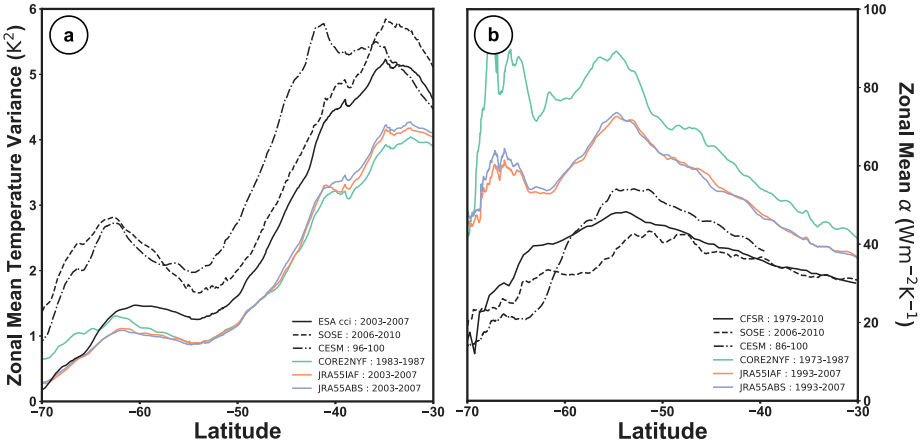

Fig. B.2. Zonal averages of (a) temperature variance and (b) α, the net air–sea heat flux feedback parameter, for the data sources and time periods shown in the legends.

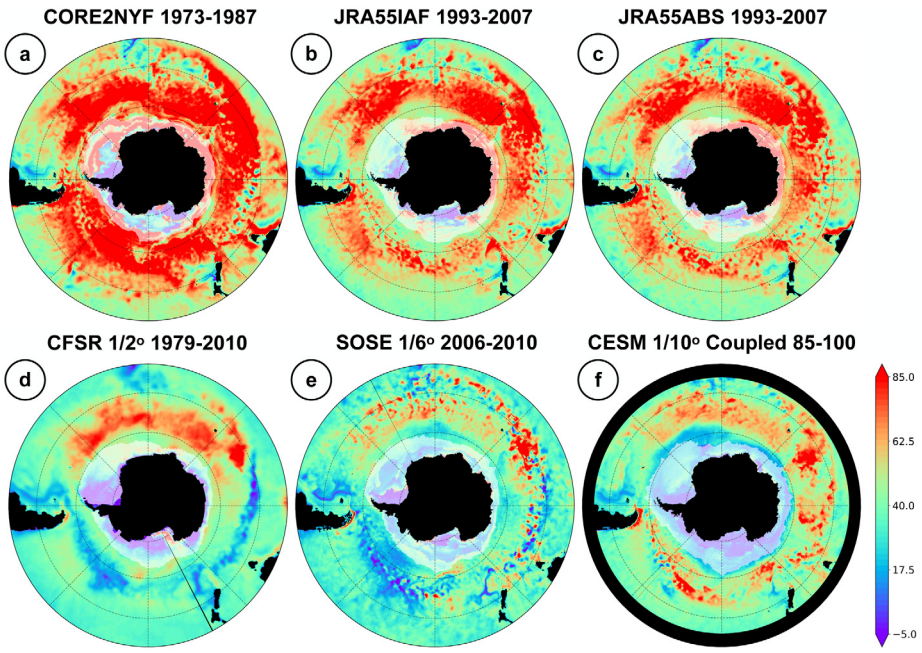

Fig. B.3. Air–sea net heat flux/SST feedback parameter, α, in W m^{-2} K^{-1} for the data sources and time periods in the panel captions.. (a) CORE2NYF, (b) JRA55IAF, (c) JRA55ABS, (d) CFSR, (e) SOSE and (f) CESM. Solid black is land, white shading is the April–May–June average ice extent. Only the domain south of 35°S is shown.

The rate at which SST anomalies are damped by air–sea interaction, α_{net} (in W m^{-2} K^{-1} with positive value indicating damping of SST anomalies) is an important parameter of the climate system. Observations indicate that α_{net} varies in space and time (Frankignoul, 1985; Frankignoul and Kestenare, 2002; Park et al., 2005) and depends on the scale of the SST anomalies themselves. For midlatitudes, α_{net} is typically $\sim$ 20 W m^{-2} K^{-1} (Frankignoul, 1985; Frankignoul et al., 1998) and recent Southern Ocean estimates (Hausmann et al., 2016a,b) suggest lower values over the ACC. This suggests weaker damping of SST anomalies over much of the Southern Ocean, with respect to the midlatitudes. Based on the estimates of temperature variance in Figs. B.1 and B.2a and the above argument, we expect our NEMO experiments to exhibit higher values of α_{net} than in the results of Hausmann et al. (2016a,b), SOSE and CESM. As a starting point, we would expect α_{net} for our NEMO models to be at least the upper bound obtained from the bulk formula, which is 20–40 W m^{-2} K^{-1} for the SO (Hausmann et al., 2016b)

To estimate α_{net} we adopt the method of Hausmann et al. (2016a), as established by Frankignoul et al. (1998) and rooted in the theoretical framework of Frankignoul and Hasselmann (1977), based on stochastic climate models. This method uses lagged covariances to separate the key role of air–sea heat fluxes in generating SST anomalies from the damping feedback. Our estimate is given by

$$\alpha_{net} = \frac{1}{n}\sum_{i=1}^{n}\frac{\overline{T'(t)\,Q'(t+i\delta t)}}{\overline{T'(t)\,T'(t+i\delta t)}}, \tag{B.1}$$

where T' and Q' are monthly SST and net surface heat flux anomalies, respectively, an overbar is a time-average over the full length of the time series and δt is one month. We construct a time series for each data source of monthly anomalies from a time average of SST and net surface heat flux over the length of that time series. In contrast to Hausmann et al. (2016a), we set $n = 2$, as we find that using $n = 3$ leads to noisy estimates of α_{net} due to low statistical significance of $\overline{T'(t)\,T'(t+i\delta t)}$ at a lag of 3 months. This may reflect the finite length of our timeseries. In locations where Student's t-test indicates that the T' autocorrelation is statistically insignificant at a lag of two months, we revert to a $n = 1$ estimate for α_{net}. We mask regions with sea-ice concentration > 0.15 in calculating α_{net}, regardless of the statistical significance of the T' autocorrelation.

For CORE2NYF, JRA55IAF and JRA55ABS we use a 15 year long time series, since we found the five years used for our other analyses to lead to lower statistical significance in the required (co)variances. We take the last 15 years of CORE2NYF, from 1973 to 1987, inclusive, and the last 15 years of JRA55ABS, from 1993 to 2007, inclusive, using this same period for JRA55IAF. This maximises the spinup time of JRA55IAF after the change from CORE2 to JRA55-do forcing, whilst also giving JRA55ABS five years to spinup its stronger eddy field after the start of the experiment. For similar reasons, we use the last 15 years of the same CESM experiments as used above. In lieu of an observational estimate we use data from the Climate Forecast System Reanalysis (CFSR) (Saha et al., 2010a,b), which uses an ocean component with a 0.25° grid spacing at the Equator, extending to 0.5° globally outside of the Tropics. We use the full length of the CFSR record, which begins in 1979 and ends in 2010, for our anomaly time series.

Maps of our α_{net} estimate for CORE2NYF, JRA55IAF and JRA55ABS are shown in Figs. B.3a–c. All three models have large areas of α_{net} in excess of 85 W m^{-2} K^{-1} extending circumpolarly around the Southern Ocean. The values are, broadly, four times the observational estimates of Hausmann et al. (2016a,b) for similar regions. Even close to Antarctica, and under the seasonal sea-ice as indicated by the white shading, the NEMO experiment estimates remain large and mostly positive. This indicates that damping of SST anomalies by net air–sea heat flux in the models is much stronger than we would expect from observations. CORE2NYF has the largest values of α_{net}, particularly over the Indo-Pacific sector. Given the otherwise similar model configuration, this must reflect some difference between the CORE2 and JRA55-do forcing sets, such as the longer time period between successive atmospheric fields.

The other three α_{net} estimates in Fig. B.3d–f correspond to CFSR, SOSE and CESM. They are all notably lower then for the NEMO experiments. As the longest time series, the CFSR estimate is probably the most statistically valid, hence its smoother spatial patterns, which its lower resolution may also contribute to. Whilst α_{net} remains large (> 60 W m^{-2} K^{-1}) over much of the Atlantic and Indian sectors, low values $\lesssim 20$ W m^{-2} K^{-1} are found in the core of the ACC over the Pacific sector. These values are more in line with the observation estimates of Hausmann et al. (2016a,b). That they are clearly an imprint of the

dynamically distinct ACC on this quantitative estimate of the heat flux feedback on SST anomalies is extremely intriguing. It could be related to the strong currents tending to advect mesoscale eddies, with their small scale anomaly pattern, largely eastward, rather than allowing clear migration north or south where their temperature would be more anomalous. We leave understanding this to future work.

With its shortest time series, the SOSE estimate of α_{net} in Fig. B.3e is the noisiest with a lot of small scale structure and frequent sign changes. Broadly speaking, and without drawing overly strong conclusions based on the short length of the time series, there is good agreement with the CFSR estimate. Large positive values are found in the Atlantic and Indian sectors and, most importantly, this is the only other estimate that shows low values of α_{net} in the core of the ACC over the Pacific sector.

As the only coupled high resolution coupled model, we could reasonably expect CESM's α_{net} to be somewhere between that of CFSR and the NEMO experiments. Accordingly, Fig. B.3f shows considerably lower values than for all the NEMO experiments. Compared to CFSR and SOSE, the peak values of α_{net} are lower, but spread over a broader area. This is borne out by the zonal mean of Fig. B.2b, which shows that the zonal mean values for CFSR, SOSE and CESM are all very similar. The general pattern, of a peak at 50–60°S and lower values towards the pole (where the estimate is seasonally masked due to ice cover) is very similar. The zonal averages for the NEMO experiments are all considerably higher, particularly for CORE2NYF. However, they continue to show the peak in α_{net} between 50–60°S, which is the general location of the minima in temperature variance, as shown in Fig. B.2a. This supports our hypothesis that the temperature variance is lower in the NEMO experiment because they are overly strongly restoring the SST to the prescribed atmospheric temperature, which results in overly strong damping of SST anomalies. They also support the minima in temperature variance being due to where the strongest damping is present, in all data sources. Whilst this argument is consistent with our arguments there are clearly subtleties; CESM has more temperature variance and a stronger α_{net} estimate than SOSE, whilst zonal asymmetry is most distinct in the CFSR estimate. There may be other effects coming into play here, such as the resolution of the ocean, the details of the bulk formulae in use and the formulation of the model (state estimate vs. coupled climate). We leave a full exploration of such effects to a future publication.

References

Adcroft, A., Campin, J.M., 2004. Rescaled height coordinates for accurate representation of free-surface flows in ocean circulation models. Ocean Model. 7, 269–284.

Adcroft, A., Hill, C., Marshall, J., 1997. Representation of topography by shaved cells in a height coordinate ocean model. J. Phys. Oceanogr. 125, 2293–2315.

Allison, L.C., Johnson, H.L., Marshall, D.P., 2011. Spin-up and adjustment of the Antarctic Circumpolar Current and global pycnocline. J. Mar. Res. 69, 167–189. http://dx.doi.org/10.1357/002224011798765330.

Barnier, B., Madec, G., Penduff, T., Molines, J., Treguier, A.M., Le Sommer, J., Beckmann, A., Biastoch, A., Böning, C., Dengg, J., Derval, C., Durand, E., Gulev, S., Remy, E., Talandier, C., Theetten, S., Maltrud, M., McClean, J., de Cuevas, B., 2006. Impact of partial steps and momentum advection schemes in a global ocean circulation model at eddy-permitting resolution. Ocean Dyn. 56, 543–567.

Bell, M.J., Peixoto, P.S., Thuburn, J., 2016. Numerical instabilities of vector-invariant momentum equations on rectangular C-grids. Q. J. R. Meteorol. Soc. 143, 563–581. http://dx.doi.org/10.1002/qj.2950.

Blanke, B., Delecluse, P., 1993. Variability of the tropical Atlantic Ocean simulated by a general circulation model with two different mixed-layer physics. J. Phys. Oceanogr. 23, 1363–1388. http://dx.doi.org/10.1175/1520--0485(1993)023<1363:VOTTAO>2.0.CO;2.

Bryden, H.L., 1979. Poleward heat flux and conversion of available potential energy in drake passage. J. Mar. Res. 37, 1–22.

Cavalieri, D.J., Parkinson, C.L., Gloerson, P., Zwally, H.J., 1996. Sea Ice Concentrations from Nimbus-7 SMMR and DMSP SSM/I-SSMIS Passive Microave Data, Version 1. NASA National Snow and Ice Data Center Distributed Active Archive Center, Boulder, Colorado, USA, http://dx.doi.org/10.5067/8GQ8LZQVL0VL, accessed 03/20..

Davies, H., 1976. A lateral boundary formulation for multi-level prediction models.. Q. J. R. Meteorol. Soc. 102, 405–418. http://dx.doi.org/10.1002/qj.49710243210.

Dawe, J.T., Thompson, L., 2006. Effect of ocean surface currents on wind stress, heat flux, and wind power input to the ocean. Geophys. Res. Lett. 33, L09604. http://dx.doi.org/10.1029/2006GL025784.

Delworth, T.L., Rosati, A., Anderson, W., Adcroft, A.J., Balaji, V., Benson, R., Dixon, K., Griffies, S.M., Lee, H.-C., Pacanowski, R.C., Vecchi, G.A., Wittenberg, A.T., Zeng, F., Zhang, R., 2012. Simulated climate and climate change in the GFDL CM2.5 high-resolution coupled climate model. J. Clim. 25, 2755–2781.

Dewar, W.K., Flierl, G.R., 1987. Some effects of the wind on rings. J. Phys. Oceanogr. 17, 1653–1667.

Donohue, K.A., Tracey, K.L., Watts, D.R., Chidichimo, M.P., Chereskin, T.K., 2016. Mean Antarctic Circumpolar Current transport measured in Drake Passage. Geophys. Res. Lett. 43, 11 760–11 767. http://dx.doi.org/10.1002/2016GL070319.

Duhaut, T.H., Straub, D.N., 2006. Wind stress dependence on ocean surface velocity: Implications for mechanical energy input to ocean circulation. J. Phys. Oceanogr. 36, 202–211.

Engerdahl, H., 1995. Use of the flow relaxation scheme in a three-dimensional baroclinic ocean model with realistic topography. Tellus 47A, 365–382. http://dx.doi.org/10.3402/tellusa.v47i3.11523.

Ferrari, R., Wunsch, C., 2009. Ocean circulation kinetic energy: Reservoirs, sources, and sinks. Annu. Rev. Fluid Mech. 41, 253–282. http://dx.doi.org/10.1146/annurev.fluid.40.111406.102139.

Ferreira, D., Marshall, J., Campin, J.M., 2010. Localization of deep water formation: Role of atmospheric moisture transport and geometrical constraints on ocean circulation. J. Clim. 23, 1456–1476.

Ferreira, D., Marshall, J., Rose, B., 2011. Climate determinism revisited: Multiple equilibria in a complex climate model. J. Clim. 24, 992–1012.

Fetterer, F., Knowles, K., Meier, W.N., Savoie, M., Windnagel, A.K., 2017. Sea Ice Index, Version 3. National Snow and Ice Data Center, Boulder, Colorado, USA. NSIDC, http://dx.doi.org/10.7265/N5K072F8, accessed 05/20..

Forget, G., Campin, J.M., Heimbach, P., Hill, C.N., Ponte, R.M., Wunsch, C., 2015. ECCO version 5: an integrated framework for non-linear inverse modeling and global ocean state estimate. Geosci. Model Dev. 8, 3071–3104. http://dx.doi.org/10.5194/gmd--8--3071--2015.

Forget, G., Campin, J.M., Heimbach, P., Hill, C.N., Ponte, R.M., Wunsch, C., 2016. ECCO version 4: Second release. http://hdl.handle.net/1721.1/102062.

Frankignoul, C., 1985. Sea surface temperature anomalies, planetary waves and air-sea feedback in the middle latitudes. Rev. Geophys. 23, 357–390. http://dx.doi.org/10.1029/RG023i004p00357.

Frankignoul, C., Czaja, A., L'Heveder, B., 1998. Air-sea feedback in the North Atlantic and surface boundary conditions for ocean models. J. Clim. 11, 2310–2324. http://dx.doi.org/10.1175/1520--0442(1998)011<2310:ASFITN>2.0.CO;2.

Frankignoul, C., Hasselmann, K., 1977. Stochastic climate models. Part II: Application to sea-surface temperature anomalies and thermocline variability. Tellus 29A, 289–305. http://dx.doi.org/10.1111/j.2153--3490.1977.tb00740.x.

Frankignoul, C., Kestenare, E., 2002. The surface heat flux feedback. Part I: Estimates from observations in the Atlantic and North Pacific. Clim. Dyn. 19, 633–647. http://dx.doi.org/10.1007/s00382-002-0252-x.

Gerdes, R., Köberle, C., Willebrand, J., 1991. The influence of numerical advection schemes on the results of ocean general circulation models. Clim. Dyn. 5, 211–226.

Gille, S.T., 2003. Float observations of the Southern Ocean. Part II: Eddy fluxes. J. Phys. Oceanogr. 33, 1182–1196.

Good, S.A., Embury, O., Bulgin, C.E., Mittaz, J., 2019. ESA Sea Surface Temperature Climate Change Initiative (SST_cci): Level 4 Analysis Climate Data Record, version 2.1. Centre for Environmental Data Analysis, http://dx.doi.org/10.5285/62c0f97b1eac4e0197a674870afe1ee6.

Goutorbe, B., Poort, J., Lucazeau, F., Raillard, S., 2011. Global heat flow trends resolved from multiple geological and geophysical proxies. Geophys. J. Int. 187, 1405–1419. http://dx.doi.org/10.1111/j.1365.246X.2011.05228.x.

Griffies, S.M., Pacanowski, R.C., Hallberg, R.W., 2000. Spurious diapycnal mixing associated with advection in a z-coordinates ocean model. Mon. Wea. Rev. 128, 538–564.

Hausmann, U., Czaja, A., 2012. The observed signature of mesoscale eddies in sea surface temperature and the associated heat transport. Deep-Sea Res. 70, 60–72.

Hausmann, U., Czaja, A., Marshall, J., 2016a. Estimates of air-sea feedbacks on sea surface temperature anomalies in the Southern Ocean. J. Clim. 29, 439–454. http://dx.doi.org/10.1175/JCLI--D--15--0015.1.

Hausmann, U., Czaja, A., Marshall, J., 2016b. Mechanisms controlling the SST air-sea heat flu feedback and its dependence on spatial scale. Clim. Dyn. 48, 1297–1307. http://dx.doi.org/10.1007/s00382--016--3142--3.

Hecht, M.W., Holland, W.R., Rasch, P.J., 1995. Upwind-weighted advection schemes for ocean tracer transport: An evaluation in a passive tracer context. J. Geophys. Res. 100, 20 763–20 778. http://dx.doi.org/10.1029/95JC01813.

Hofmann, M., Morales Maqueda, M.A., 2006. Performance of a second-order moments advection scheme in an Ocean General Circulation Model. J. Geophys. Res. 111, C05006. http://dx.doi.org/10.1029/2005JC003279.

Hogg, A.M., Dewar, W.K., Killworth, P.D., Blundell, J.R., 2003. A quasi-geostrophic coupled model (Q-GCM). Mon. Wea. Rev. 131, 2261–2278. http://dx.doi.org/10.1175/1520--0493(2003)131<2261:AQCMQ>2.0.CO;2.

Hogg, A.M., Meredith, M.P., Chambers, D.P., Abrahamsen, E.P., Hughes, C.W., Morrison, A.K., 2015. Recent trends in the Southern Ocean eddy field.. J. Geophys. Res. 120, 257–267. http://dx.doi.org/10.1002/2014JC010470.

Hollingsworth, A., Kållberg, P., Renner, V., Burridge, D.M., 1983. An internal symmetric computational instability.. Q. J. R. Meteorol. Soc. 109, 417–428. http://dx.doi.org/10.1002/qj.49710946012.

Hughes, C.W., Wilson, C., 2008. Wind work on the geostrophic ocean circulation: An observational study of the effect of small scales in the wind stress. J. Geophys. Res. 113, C02016. http://dx.doi.org/10.1029/2007JC004371.

Hutchinson, D.K., Hogg, A.M., Blundell, J.R., 2010. Southern ocean response to relative velocity wind stress forcing.. J. Phys. Oceanogr. 40, 326–339.

Jayne, S.R., Marotzke, J., 2002. The oceanic eddy heat transport.. J. Phys. Oceanogr. 32, 3328–3345.

Johnson, G.C., Bryden, H.L., 1989. On the size of the Antarctic Circumpolar Current. Deep-Sea Res. 36, 39–53.

Karsten, R., Jones, H., Marshall, J., 2002. The role of eddy transfer in setting the stratification and transport of a circumpolar current. J. Phys. Oceanogr. 32, 39–54.

Kjellson, J., Holland, P.R., Marshall, G.J., Mathiot, P., Aksenov, Y., Coward, A.C., Bacon, S., Megann, A.P., Ridley, J., 2015. Model sensitivity of the Weddell and Ross seas, Antarctica, to vertical mixing and freshwater forcing. Ocean Model. 94, 141–152. http://dx.doi.org/10.1016/j.ocemod.2015.08.003.

Large, W.G., Yeager, S.G., 2004. Diurnal to decadal global forcing for ocean and seaice models: The data sets and climatologies. Technical Report NCAR/TN-4600+STR, NCAR, University Corporation for Atmospheric Research, http://dx.doi.org/10.5065/D6KK98Q6.

Large, W.G., Yeager, S.G., 2009. The global climatology of an interannually varying air-sea flux data set. Clim. Dyn. 33, 341–364. http://dx.doi.org/10.1007/s00382--008--0441--3.

Le Sommer, J., Penduff, T., Theetten, S., Madec, G., Barnier, B., 2009. How momentum advection schemes influence current-topography interactions at eddy permitting resolution. Ocean Model. 29, 1–14.

Lin, X., Zhai, X., Wang, Z., Munday, D.R., 2018. Mean, variability, and trend of Southern Ocean wind stress: Role of wind fluctuations. J. Clim. 31, 3557–3573. http://dx.doi.org/10.1175/JCLI--D--17--0481.1.

Luo, J.J., Masson, S., Roeckner, E., Madec, G., Yamagata, T., 2005. Reducing climatology bias in an ocean-atmosphere CGCM with improved coupling physics. J. Clim. 18, 2344–2360.

Marshall, J., Ferreira, D., Campin, J.M., Enderton, D., 2007. Mean climate and variability of the atmosphere and ocean on an aquaplanet. J. Atmos. Sci. 64, 4270–4286.

Marshall, J., Jones, H., Karsten, R., Wardle, R., 2002. Can eddies set ocean stratification? J. Phys. Oceanogr. 32, 26–38.

Marshall, J., Olbers, D., Ross, H., Wolf-Gladrow, D., 1993. Potential vorticity constraints on the dynamics and hydrography of the Southern Ocean. J. Phys. Oceanogr. 23, 465–487.

Marshall, J., Radko, T., 2003. Residual-mean solutions for the Antarctic Circumpolar Current and its associated overturning circulation. J. Phys. Oceanogr. 33, 2341–2354.

Marshall, J., Speer, K., 2012. Closure of the meridional overturning circulation through Southern Ocean upwelling. Nature Geo. 5, 171–180.

Marshall, J., Whitehead, J.A., Yates, T., 1994. Laboratory and numerical experiments in oceanic convection. In: Malanotte-Rizzoli, P., Robinson, A.R. (Eds.), Ocean Process in Climate Dynamics: Global and Mediterranean Examples. Kluwer Academic Publishers, pp. pages 173–201.

Mazloff, M.R., Heimbach, P., Wunsch, C., 2010. An eddy-permitting Southern Ocean State Estimate. J. Phys. Oceanogr. 40, 880–899. http://dx.doi.org/10.1175/2009JPO4236.1.

Meijers, A.J., Bindoff, N.L., Roberts, J.L., 2007. On the total, mean, and eddy heat and freshwater transports in the southern hemisphere of a $\frac{1}{8}^{\circ} \times \frac{1}{8}^{\circ}$ global ocean model.. J. Phys. Oceanogr. 37, 277–295.

Merchant, C.J., Embury, O., Bulgin, C.E., Block, T., Corlett, G.K., Fiedler, E., Good, S.A., Mittaz, J., Rayner, N.A., Berry, D., Eastwood, S., Taylor, M., Tsushima, Y., Waterfall, A., Wilson, R., Donlon, C., 2019. Satellite-based time-series of sea-surface temperature since 1981 for climate applications. Sci. Data 6, 1–18. http://dx.doi.org/10.1038/s41597--019--0236--x.

Meredith, M.P., Hogg, A.M., 2006. Circumpolar response of Southern Ocean eddy activity to a change in the Southern Annular Mode. Geophys. Res. Lett. 33, L16608. http://dx.doi.org/10.1029/2006GL026499.

Meredith, M.P., Woodworth, P.L., Chereskin, T.K., Marshall, D.P., Allison, L.C., Bigg, G.R., Donohue, K., Heywood, K.J., Hughes, C.W., Hibbert, A., Hogg, A.M., Johnson, H.L., King, B.A., Leach, H., Lenn, Y., Morales-Maqueda, M.A., Munday, D.R., Naveira-Garabato, A.C., Provost, C., Sprintall, J., 2011. Sustained monitoring of the southern ocean at drake passage: past achievements and future priorities. Rev. Geophys. 49, RG4005. http://dx.doi.org/10.1029/2010RG000348.

Morales Maqueda, M.A., Holloway, G., 2006. Second-order moment advection scheme applied to Arctic Ocean simulation. Ocean Model. 14, 197–221. http://dx.doi.org/10.1016/j.ocemod.2006.05.003.

Morrison, A.K., Hogg, A.M., Ward, M.L., 2011. Sensitivity of the Southern Ocean overturning circulation to surface buoyancy forcing. Geophys. Res. Lett. 38, L14602. http://dx.doi.org/10.1029/2011GL048031.

Munday, D., Harle, J., Nurser, A., Coward, A., 2021. 1/12 degree Nucleus for European Modelling of the Ocean (NEMO) model of the Southern Ocean: CORE2 normal year forced control run (1951-1987). NERC EDS British Oceanographic Data Centre, http://dx.doi.org/10.5285/2e982e6692e3427dbe35e64ad9dee12d, 17 September 2021.

Munday, D.R., Harle, J., Nurser, A., Coward, A., 2021. 1/12 degree Nucleus for European Modelling of the Ocean (NEMO) model of the Southern Ocean: JRA55-do interannually-varying forced control run (1978 - 2017). NERC EDS British Oceanographic Data Centre, 17 September 2021. doi: catalogue.ceda.ac.uk/uuid/67ad0c489e2b4d18aa152e78f28ae0c0.

Munday, D.R., Zhai, X., 2015. Sensitivity of Southern Ocean circulation to wind stress changes: Role of relative wind stress. Ocean Model. 95, 15–24. http://dx.doi.org/10.1016/j.ocemod.2015.08.004.

Munday, D.R., Zhai, X., 2017. The impact of atmospheric storminess on the sensitivity of Southern Ocean circulation to wind stress changes. Ocean Model. 115, 14–26. http://dx.doi.org/10.1016/j.ocemod.2017.05.005.

Munday, D., Zhai, X., 2021. 1/12 degree Nucleus for European Modelling of the Ocean (NEMO) model of the Southern Ocean: JRA55-do with absolute wind stress experiment (1988 - 2007). NERC EDS British Oceanographic Data Centre, 17 September 2021. doi: catalogue.ceda.ac.uk/uuid/aa4106a7a35246dfb84fb925a7d65650.

Munk, W.H., Palmén, E., 1951. Note on the dynamics of the Antarctic Circumpolar Current. Tellus 3, 53–55.

NEMO System Team, 2019. NEMO Ocean Engine. In: Number 27 in Scientific Notes of Climate Modelling Center, Zenodo, Institut Pierre-Simon Laplace (IPSL), http://dx.doi.org/10.5281/zenodo.146816.

Nurser, A.J., Lee, M.M., 2004a. Isopycnal averaging at constant height. Part I: The formulation and a case study. J. Phys. Oceanogr. 34, 2721–2739.

Nurser, A.J., Lee, M.M., 2004b. Isopycnal averaging at constant height. Part II: Relating to the residual streamfunction in Eulerian space. J. Phys. Oceanogr. 34, 2740–2755.

Pacanowski, R.C., 1987. Effect of equatorial currents on surface stress. J. Phys. Oceanogr. 17, 833–838.

Park, S., Deser, C., Alexander, M.A., 2005. Estimation of the surface heat flux response to sea surface temperature anomalies over the global oceans. J. Clim. 18, 4582–4599. http://dx.doi.org/10.1175/JCLI3521.1.

Penduff, T., Juza, M., Brodeau, L., Smith, G.C., Barnier, B., Molines, J.M., Treguier, A.M., Madec, G., 2010. Impact of global ocean model resolution on sea-level variability with emphasis on interannual time scales. Ocean Sci. 6, 269–284.

Penduff, T., Le Sommer, J., Barnier, B., Treguier, A.M., Molines, J.M., Madec, G., 2007. Influence of numerical schemes on current-topography interactions in 1/4° global ocean simulations. Ocean Sci. 3, 509–524.

Prather, M.J., 1986. Numerical advection by conservation of second-order moments.. J. Geophys. Res. 91, 6671–6681.

Redi, M.H., 1982. Oceanic isopycnal mixing by coordinate rotation.. J. Phys. Oceanogr. 12, 1154–1158.

Renault, L., Marchisiello, P., Masson, S., McWilliams, J.C., 2019. Remarkable control of western boundary currents by *eddy killing*, a mechanical air-sea coupling process. Geophys. Res. Lett. 46, 2743–2751. http://dx.doi.org/10.1029/2018GL081211.

Renault, L., McWilliams, J.C., Penven, P., 2017. Modulation of the Agulhas Current retroflection and leakage by oceanic current interaction with the atmosphere in coupled simulations. J. Phys. Oceanogr. 47, 2077–2100. http://dx.doi.org/10.1175/JPO--D--16--0168.1.

Renault, L., Molemaker, M.J., Gula, J., Masson, S., McWilliams, J.C., 2016a. Control and stabilization of the Gulf Stream by oceanic current interaction with the atmosphere. J. Phys. Oceanogr. 46, 3439–3453. http://dx.doi.org/10.1175/JPO--D--0115.1.

Renault, L., Molemaker, M.J., McWilliams, J.C., Shchepetkin, A.F., Lemarié, F., Chelton, D., Illig, S., Hall, A., 2016b. Modulation of wind work by oceanic current interaction with the atmosphere. J. Phys. Oceanogr. 46, 1685–1704. http://dx.doi.org/10.1175/JPO--D--15--0232.1.

Roquet, F., Madec, G., McDougall, T.J., Barker, P.M., 2015. Accurate polynomial expressions for the density and specfic volume of seawater using the TEOS-10 standard. J. Phys. Oceanogr. 45, 2564–2579. http://dx.doi.org/10.1016/j.ocemod.2015.04.002.

Roquet, F., Wunsch, C., Madec, G., 2011. On the patterns of wind-power input to the ocean circulation.. J. Phys. Oceanogr. 41, 2328–2342. http://dx.doi.org/10.1175/JPO--D--11--024.1.

Rousset, C., Vancoppenolle, M., Madec, G., Fichefet, T., Flavoni, S., Barthélemy, A., Benshila, R., Chanit, J., Levy, C., Masson, S., Vivier, F., 2015. The Louvain-La-Neuve sea ice model LIM3.6: global and regional capabilities. Geosci. Model Dev. 8, 2991–3005. http://dx.doi.org/10.5194/gmd--8--2991--2015.

Saha, S., Moorthi, S., Pan, H.-L., Wu, X., Wang, J., Nadiga, S., Tripp, P., Kistler, R., Woollen, J., Behringer, D., Liu, H., Stokes, D., Grumbine, R., Gayno, G., Wang, J., Hou, Y.-T., Chuang, H.-Y., Juang, H.-M.H., Sela, J., Iredell, M., Treadon, R., Kleist, D., Delst, P.V., Keyser, D., Derber, J., Ek, M., Meng, J., Wei, H., Yang, R., Lord, S., van den Dool, H., Kumar, A., Wang, W., Long, C., Chelliah, M., Xue, Y., Huang, B., Schemm, J.-K., Ebisuzaki, W., Lin, R., Xie, P., Chen, M., Zhou, S., Higgins, W., Zou, C.-Z., Liu, Q., Chen, Y., Han, Y., Cucurull, L., Reynolds, R.W., Rutledge, G., Goldberg, M., 2010a. The NCEP climate forecast system reanalysis. Bull. Amer. Met. Soc. 91, 1015–1057. http://dx.doi.org/10.1175/2010BAMS3001.1.

Saha, S., Moorthi, S., Pan, H.-L., Wu, X., Wang, J., Nadiga, S., Tripp, P., Kistler, R., Woollen, J., Behringer, D., Liu, H., Stokes, D., Grumbine, R., Gayno, G., Wang, J., Hou, Y.-T., Chuang, H.-Y., Juang, H.-M.H., Sela, J., Iredell, M., Treadon, R., Kleist, D., Delst, P.V., Keyser, D., Derber, J., Ek, M., Meng, J., Wei, H., Yang, R., Lord, S., van den Dool, H., Kumar, A., Wang, W., Long, C., Chelliah, M., Xue, Y., Huang, B., Schemm, J.-K., Ebisuzaki, W., Lin, R., Xie, P., Chen, M., Zhou, S.,

Higgins, W., Zou, C.-Z., Liu, Q., Chen, Y., Han, Y., Cucurull, L., Reynolds, R.W., Rutledge, G., Goldberg, M., 2010b. NCEP Climate Forecast System Reanalysis (CFSR) Monthly Products, January 1979 to December 2010. Research Data Archive at the National Center for Atmospheric Research, Computational and Information Systems Laboratory, Boulder CO, http://dx.doi.org/10.5065/D6DN438J.

Sallée, J.B., Morrow, R., Speer, K., 2008. Eddy heat diffusion and Subantarctic Mode Water formation.. Geophys. Res. Lett. 35, L05607. http://dx.doi.org/10.1029/2007GL032827.

Scott, R.B., Xu, Y., 2009. An update on the wind power input to the surface geostrophic flow of the World Ocean. Deep-Sea Res. 56, 295–304.

Seo, H., 2017. Distinct influence of air-sea interactions mediated by mesoscale sea surface temperature and current in the Arabian Sea. J. Clim. 30, 8061–8080. http://dx.doi.org/10.1175/JCLI-D-16-0834.1.

Seo, H., Miller, A.J., Norris, J.R., 2016. Eddy-wind interaction in the California Current System: Dynamics and impacts. J. Phys. Oceanogr. 46, 439–459. http://dx.doi.org/10.1175/JPO--D--15--0086.1.

Seo, H., Subramanian, A.C., Song, H., Chowdary, J.S., 2019. Coupled effects of ocean current on wind stress in the Bay of Bengal: Eddy energetics and upper ocean stratification. Deep-Sea Res. 168, 104617. http://dx.doi.org/10.1016/j.dsr2.2019.07.005.

Shchepetkin, A.F., McWilliams, J.C., 2005. The regional oceanic modeling system (ROMS) - a split-explicit, free-surface, topography-following-coordinate ocean model. Ocean Model. 9, 347–404. http://dx.doi.org/10.1016/j/ocemod.2004.08.002.

Simmons, H.L., Jayne, S.R., St. Laurent, L.C., Weaver, A.J., 2004. Tidally driven mixing in a numerical model of the ocean general circulation. Ocean Model. 6, 245–263. http://dx.doi.org/10.1016/S1463--5003(03)00011--8.

Small, R.J., Bacmeister, J., Bailey, D., Baker, A., Bishop, S., Bryan, F., Caron, J., Dennis, J., Gent, P., Hsu, H., Jochum, M., Lawrence, D., Muñoz, E., diNezio, P., Scheitlin, T., Tomas, R., Tribbia, J., Tseng, Y., Vertenstein, M., 2014. A new synoptic scale resolving global climate simulation using the Community Earth System Model. J. Adv. Model. Earth Sys. 6, 1065–1094. http://dx.doi.org/10.1002/2014MS000363.

Song, H., Marshall, J., McGillicuddy, Jr., D.J., Seo, H., 2020. Impact of current-wind interaction on vertical processes in the Southern Ocean. J. Geophys. Res. 125, e2020JC016046.

Stammer, D., 1998. On eddy characteristics, eddy transports, and mean flow properties.. J. Phys. Oceanogr. 28, 727–739.

Stone, P.H., 1978. Constraints on dynamical transports of energy on a spherical planet.. Dyn. Atmos. Oceans 2, 123–139.

Tsujino, H., Urakawa, S., Nakano, H., Small, R.J., Kim, W.M., Yeager, S.G., Danabasoglu, G., Suzuki, T., Bamber, J.L., M, B., Böning, C.W., Bozec, A., Chassignet, E.P., Curchitser, E., Boeira Dias, F., Durack, P.J., Griffies, S.M., Harada, Y., Ilicak, M., Josey, S.A., Kobayashi, C., Kobayashi, S., Komuro, Y., Large, W.G., Le Sommer, J., Marsland, S.J., Masina, S., Scheinert, M., Tomita, H., Valdivieso, M., Yamazaki, D., 2018. JRA-55 based surface dataset for driving ocean-sea-ice models (JRA55-do). Ocean Model. 130, 79 – 139. http://dx.doi.org/10.1016/j.ocemod.2018.07.002.

van Leer, B., 1973. Towards the ultimate conservative difference scheme i. the quest of monotonicity. In: Lecture Notes in Physics. Proceedings of the Third International Conference on Numerical Methods in Fluid Mechanics.. Springer.

van Leer, B., 1974. Towards the ultimate conservative difference scheme. II. Monotonicity and conservation combined in a second-order scheme.. J. Comput. Phys. 14, 361–370. http://dx.doi.org/10.1016/0021--9991(74)90019--9.

van Leer, B., 1977a. Towards the ultimate conservative difference scheme. III. Upstream-centered finite-difference schemes for ideal compressible flow.. J. Comput. Phys. 23, 263–275. http://dx.doi.org/10.1016/0021--9991(77)90094--8.

van Leer, B., 1977b. Towards the ultimate conservative difference scheme. IV. A new approach to numerical convection. J. Comput. Phys. 23, 276–299. http://dx.doi.org/10.1016/0021--9991(77)90095--X.

van Leer, B., 1979. Towards the ultimate conservative difference scheme. V. A second-order sequel to Godunov's method. J. Comput. Phys. 32, 101–136. http://dx.doi.org/10.1016/0021--0001(79)90145--1.

van Leer, B., 1997. Towards the ultimate conservative difference scheme.. J. Comput. Phys. 32, 229–248. http://dx.doi.org/10.1006/jcph.1997.5704.

Vancoppenolle, M., Fichefet, T., Goose, H., Bouillon, S., Madec, G., Morales Maqueda, M., 2009. Simulating the mass balance and salinity of arctic and antarctic sea ice. 1. Model description and validation. Ocean Model. 27, 33–53. http://dx.doi.org/10.1016/j.ocemod.2008.10.005.

Wang, W., Huang, R.X., 2004a. Wind energy input to the Ekman layer.. J. Phys. Oceanogr. 34, 1267–1275.

Wang, W., Huang, R.X., 2004b. Wind energy input to the surface waves.. J. Phys. Oceanogr. 34, 1276–1280.

Warren, B.A., 1999. Approximating the energy transport across oceanic sections.. J. Geophys. Res. 104, 7915–7919.

Wu, Y., Zhai, X., Wang, Z., 2017. Decadal-mean impact of including ocean surfaces currents in bulk formulas on surface air-sea fluxes and ocean general circulation. J. Clim. 30, 9511–9525. http://dx.doi.org/10.1175/JCLI--D--17--0001.1.

Wunsch, C., 1998. The work done by the wind on the oceanic general circulation.. J. Phys. Oceanogr. 28, 2332–2340.

Wunsch, C., Ferrari, R., 2004. Vertical mixing, energy, and the general circulation of the oceans.. Annu. Rev. Fluid Mech. 36, 281–314.

Wunsch, C., Heimbach, P., 2008. How long to oceanic tracer and proxy equilibrium? Quat. Sci. Rev. 27, 637–651.

Zhai, X., Greatbatch, R.J., 2007. Wind work in a model of the northwest atlantic ocean. Geophys. Res. Lett. 34, L04606. http://dx.doi.org/10.1029/2006GL028907.

Zhai, X., Greatbatch, R.J., Eden, C., Hibiya, T., 2009. On the loss of wind-induced near-inertial energy to turbulent mixing in the upper ocean. J. Phys. Oceanogr. 39, 3040–3045.

Zhai, X., Johnson, H.L., Marshall, D.P., Wunsch, C., 2012. On the wind power input to the ocean general circulation. J. Phys. Oceanogr. 42, 1357–1365.